Master Thesis

Thermo-optical simulation of a Star Receiver concept with molten nitrate salts

Computational mechanics – M. Sc.

Written by:

Shanmukha Teja Balusu

Matriculation-No. 3077274

Date	12.10.2020
Written at	German Aerospace Center (DLR) Institute for Solar Research
Supervisor	Dipl.-Ing. Cathy Frantz (DLR, Institute for Solar Research)
Examinar	1. Prof. Dr.- Ing.habil. Jörg Schröder 2. M.Sc. Sascha Maassen (University of Duisburg-Essen, Institute for Mechanics)

UNIVERSITÄT DUISBURG ESSEN

Open-Minded

DLR

Versicherung an Eides Statt

Ich versichere an Eides statt durch meine untenstehende Unterschrift,

- dass ich die vorliegende Arbeit - mit Ausnahme der Anleitung durch die Betreuer - selbstständig ohne fremde Hilfe angefertigt habe und

- dass ich alle Stellen, die wörtlich oder annähernd wörtlich aus fremden Quellen entnommen sind, entsprechend als Zitate gekennzeichnet habe und

- dass ich ausschließlich die angegebenen Quellen (Literatur, Internetseiten, sonstige Hilfsmittel) verwendet habe und

- dass ich alle entsprechenden Angaben nach bestem Wissen und Gewissen vorgenommen habe, dass sie der Wahrheit entsprechen und dass ich nichts verschwiegen habe.

Mir ist bekannt, dass eine falsche Versicherung an Eides Statt nach § 156 und nach § 163 Abs. 1 des Strafgesetzbuches mit Freiheitsstrafe oder Geldstrafe bestraft wird.

Ort, Datum	Unterschrift

Acknowledgement

I would like to thank all the people who have supported me during this thesis.

I would like to express my sincere gratitude to my supervisor Ms. Cathy Frantz at DLR for her continuous guidance, encouragement and motivating me throughout the thesis. She was very enthusiastic to assist in any way she could and It was pleasure working with her.

I would like to thank my supervisor Mr. Sascha Maassen at the University of Duisburg-Essen for his valuable suggestions and incredible support during my thesis.

Finally, I wish to thank my parents and friends for their continuous support and motivation throughout my study.

Abstract

Concentrated Solar Power plants can be the backbone of future energy supply due to its clean, affordable and bulk supply of energy. Solar Tower plants with nitrate salts are one of the most promising technologies because of cost effective storage and ability to provide dispatchable supply of electricity. In Solar Tower plants, the receiver is an essential component that transforms the solar radiation into heat. The receiver must withstand high working temperature and high heat flux densities. Therefore, it is necessary to optimize the design of the receiver. The aim of this work is to study the thermo-optical behavior of the new receiver design known as STAR receiver concept, with molten nitrate salts (60 % $NaNO_3$ + 40 % KNO_3) as a heat transfer fluid. In the Star receiver, absorber tubes are arranged in three cantilevers which are inclined at 120° to each other and the absorber tubes are irradiated on both the sides, for the solar radiation. Analytical and numerical models are implemented to discuss the thermo-optical efficiency of the Star receiver concept. A ray tracing software known as SPRAY is used to trace the solar radiation reflected by a field of mirrors (known as heliostats) on the receiver surface to obtain the data of heat flux densities. The parameters which influence the optical efficiency such as the power reflected by the heliostats, power incident on the receiver and the solar absorptance of the receiver geometry are determined. Based on the aiming of heliostats, the concentration of heat flux densities on the receiver surface is obtained and this data is further used in the thermal evaluation of the receiver. The parameters which influence the thermal efficiency of the receiver will also be discussed such as heat flux densities, temperature distribution, mass flow rate and the thermal losses such as radiation and convection losses. Based on the Finite Element Method, a Steady-State thermal model of the Star receiver is analyzed in ANSYS software. The thermal simulation is carried out to determine the local salt temperature, the peak heat flux required to reach the desired output temperature and the thermal losses occurred in the receiver for the evaluation of thermo-optical efficiency of the model. A mean heat flux of 0.34 MW/m^2 is required to reach the desired outlet salt temperature of 565 °C. The solar absorptance of the Star receiver is 96 % and the spillage losses are around 14.6 %. The radiation, convection and reflection losses to ambient accounts for 2.8 %, 1.2 % and 4 % respectively, so the thermo-optical efficiency of the Star receiver without considering spillage losses is 92 % in contrast to 88 % in the External receiver (where only one side of the absorber tubes are irradiated). And the overall thermo-optical efficiency (the power absorbed by the salt power reaching the receiver region) of the Star receiver is 79 %, whereas in the External receiver is 86 %.

List of Figures

Figure 1: Crescent Dunes solar power plant at Nevada, United States [5]. 1
Figure 2: Parabolic Trough collector [7]. 2
Figure 3: Linear Fresnel collector [7]. 2
Figure 4: Solar Dish [7]. 2
Figure 5: Solar Tower plant [7]. 2
Figure 6: Schematic diagram of Solar plant [10]. 4
Figure 7: External tubular receiver [16]. 5
Figure 8: External receiver and Cavity receiver [6]. 6
Figure 9: Solar Two receiver arrangement [17]. 7
Figure 10: Receiver designs for macro and meso [20]. 8
Figure 11: Star receiver with a central pylon [6]. 8
Figure 12: Star receiver. 9
Figure 13: Area of External and Star receiver [6]. 10
Figure 14: Losses in the receiver [22]. 11
Figure 15: Data Flow for the analysis. 16
Figure 16: Orientation of Star receiver. 17
Figure 17: Star receiver. 18
Figure 18: Heliostats distribution around the Star receiver [22]. 19
Figure 19: Schematic representation of boundary conditions. 20
Figure 20: Heat transfer coefficient as a function of wind speed [19]. 21
Figure 21: Convection to ambient. 22
Figure 22: Radiation boundary condition. 22
Figure 23: Mass flow in Star receiver. 23
Figure 24: Heat transfer coefficients along the length. 26
Figure 25: Convection to salt. 27
Figure 26: Heat flux on the Absorber panels. 27
Figure 27: Mesh study. 29
Figure 28: Maximum temperature on the absorber tubes. 30
Figure 29: View factor. 31
Figure 30: Inlet salt temperature of each panel. 35
Figure 31: Temperature of flow threads. 35
Figure 32: Efficiency with and without enclosures. 36
Figure 33 : Heat losses in the receiver. 37
Figure 34: Receiver efficiency as a function of solar load. 38
Figure 35: Losses during part load. 39
Figure 36: Receiver efficiency as a function of solar load and wind velocity. 40
Figure 37: Losses based on wind velocities. 40
Figure 38: Thermo-optical efficiencies of Star and External receiver [16]. 42
Figure 39: Losses in Star and External receiver. 43
Figure 40: Mesh along axial and circumferential direction. 48
Figure 41: Heat transfer coefficients of panel 1. 48
Figure 42: Heat transfer coefficients of panel 2. 49
Figure 43: Heat transfer coefficients of panel 3. 49

Figure 44: Heat transfer coefficients of panel 4. 50
Figure 45: Heat transfer coefficients of panel 5. 50
Figure 46: Heat transfer coefficients of panel 6. 51
Figure 47: Heat transfer coefficients of panel 7. 51
Figure 48: Heat transfer coefficients of panel 8. 52

List of Tables

Table 1: Performance of CSP technologies [8], [1]. 3
Table 2: Central receiver system with molten salt [8], [5], [9]. 3
Table 3: Absorber area in Star receiver [6] 9
Table 4: Peak flux and outlet temperature of heat transfer media [5]. 12
Table 5: Geometry details 18
Table 6: Material details. 20
Table 7: Input of mass flow. 24
Table 8: View factor details. 31
Table 9: Comparison of thermal losses. 32
Table 10: Intercept efficiency. 33
Table 11: Solar absorptance. 34
Table 12: Aiming efficiency. 34
Table 13: Efficiency of the Star receiver. 41

Nomenclature

Symbols	Units	Description
A	m^2	Area
T_w	K	Temperature of the wall
T_f	K	Temperature of the fluid
σ	$W/(m^2 K^4)$	Stephan's Boltzmann constant
ε	-	Emissivity of the body
Nu	-	Nusselt number
Re	-	Reynolds number
u	m/s	Flow velocity of fluid
D_i	m	Inner diameter of the tube
v	m^2/s	Kinematic viscosity
Pr	-	Prandtl number
L	m	Length of the tube
θ	°C	Nodal temperature
q	W/m^2	Heat flux
T_{w_in}	°C	Temperature of the inner wall
T_{w_out}	°C	Temperature of the outer wall
T_{salt}	°C	Temperature of the salt
T_{amb}	°C	Temperature at the ambient
Q_{Conv}	W	Heat convection to the salt
Q_{Solar}	W	Heat incident on the tubes
Q_{Conv_amb}	W	Heat convection to the ambient
Q_{Rad_amb}	W	Heat radiation to the ambient
C_p	J/(kg K)	Specific heat capacity
$\dot{m}$	kg/s	Mass flow rate
H	m	Length of the tube
$P_{abs,\ salt}$	W	Power absorbed by the salt
P_{spill}	W	Power loss due to spillage
P_{ther}	W	Thermal losses

P_{ref_amb}	W	Power lost due to reflection to the ambient
P_{conv_amb}	W	Power lost due to convection to the ambient
P_{IR_amb}	W	Power lost due to infrared radiation to the ambient
$P_{entering\ aperture,\ aiming}$	W	Power entering the aperture with aiming on complete receiver
$P_{entering\ aperture,\ no\ aiming}$	W	Power entering the aperture with aiming on center of the receiver
$L_{IR,\ amb}$	W	Infrared losses to ambient
$L_{Conv,\ amb}$	W	Convection losses to ambient
$v_{wind,\ R}$	m/s	Wind velocity around the receiver
$v_{wind,\ H}$	m/s	Wind velocity around the heliostats
F_{ij}	-	View factor
H_{Tower}	m	Height of the receiver tower
dt/dx	K/m	Temperature gradient
$T_{s,\ in}$	°C	Inlet temperature of the salt
$T_{s,\ out}$	°C	Outlet temperature of the salt
L_A	m	Length of surface A
L_B	m	Length of surface B
L_C	m	Length of surface C
$F_{A\text{-}C}$	-	View factor A to C
$P_{incident\ on\ receiver\ aperture}$	W	Power incident on the receiver aperture
P_{RecReg}	W	Power entering the receiver region
$P_{absorbed\ by\ the\ absorber\ tubes}$	W	Power absorbed by the absorber tubes

Greek symbols	Units	Description
λ	W/(m K)	Thermal conductivity
α	W/(m^2 K)	Heat transfer coefficient
α_{abs}	-	Absorptance
η_{aim}	-	Aiming efficiency
$\eta_{thermo-optical}$	-	Thermo-optical efficiency
$\eta_{overall\ thermo-optical}$	-	Overall thermo-optical efficiency
ε	-	Emissivity

Abbreviations

FEM	Finite Element Method
CSP	Concentrating Solar Power
CRS	Central Receiver Systems
HTF	Heat Transfer Fluid
FEA	Finite Element Analysis

Table of Contents

1 Introduction 1

2 Fundamentals 2
2.1 Solar Tower plant 3
2.2 Heliostats (Collector system) 4
2.2.1 Heat flux 4
2.3 Receiver System 5
2.3.1 Description 5
2.3.2 Receiver concept 5
2.3.3 Receiver Design 6
2.3.4 New geometries of receiver 7
2.3.5 Star receiver 8
2.3.6 Receiver efficiency 10
2.4 Material 11
2.5 Heat Transfer Fluid (HTF) 12

3 Theoretical background 13
3.1 Heat conduction 13
3.2 Heat convection 13
3.3 Heat radiation 13
3.3.1 View factor 14
3.4 Finite Element Method (FEM) 14
3.5 Raytracing 15

4 Thermo-optical model of the STAR receiver 16
4.1 Receiver configuration 17
4.2 Raytracing (Optical model) 19
4.3 Thermal FEM model 19
4.3.1 Material properties 20
4.3.2 Convection to ambient 20
4.3.3 Radiation to ambient 22
4.3.4 Mass flow 23
4.3.5 Convection to the HTF 25
4.3.5.1 Velocity of HTF 25
4.3.5.2 Reynolds number 25
4.3.5.3 Nusselt number 26
4.4 Heat flux 27
4.5 Summary of assumptions 28

5 Quality control 29
5.1 Mesh study 29
5.1.1 Temperature 30
5.2 Analytical results 30

5.2.1 View factor 30
5.2.2 Thermal losses 31

6 Results 33
6.1 Results of the optical simulation 33
6.1.1 Intercept efficiency 33
6.1.2 Solar absorptance 33
6.1.3 Aiming efficiency 34
6.2 Results of the thermal simulation 34
6.2.1 The efficiency of the receiver 36
6.2.2 Heat losses 37
6.2.3 Receiver efficiency as a function of solar load 38
6.2.4 Receiver efficiency as a function of wind velocities 39
6.3 Overall thermo-optical efficiency 41

7 Comparison and discussion 42

8 Conclusion 44

9 Bibliography 45

10 Appendix 48
10.1 Mesh 48
10.2 Heat transfer coefficients 48

1 Introduction

There is a great need to develop cost-competitive renewable energy sources because the supply of fossil fuels is depleting and the impact of CO_2 emissions on the global climate is increasing. So, achieving sufficient supplies of clean energy for the future is a great challenge. Concentrated Solar Power (CSP) is a promising renewable source of energy because it depends on the biggest source of energy i.e., the Sun, which emits more energy on to earth than the energy consumed on the earth [1]. Furthermore, it can provide cost-effective technologies because it captures and stores the Sun's energy at lower costs. Solar Tower plants are one of the most promising CSP technology due to its higher operating temperature to achieve higher electricity production efficiencies [2]. In the Solar Tower plant, the receiver is mounted on the top of a central tower and surrounded by a large field of mirrors (heliostats) to reflect sun rays on it. The primary function of the receiver-heliostat system is to convert the incident solar radiation on the heliostat field into thermal heat with the highest possible efficiency [3]. The central receiver system with molten nitrate salts ($NaNO_3$ + KNO_3) as heat transfer fluid (HTF) is currently among the most relevant CSP technologies due to the possibility to include thermal storage for several hours, which helps to generate electricity without sunlight [4].

Figure 1: Crescent Dunes solar power plant at Nevada, United States [5].

Receivers are expensive, which accounts for around 20% of the total investment of Solar Tower plant and its efficiency impacts entire power production, so the design of the receiver must be efficient to have a good thermal performance to reduce the costs. Star receiver is a promising receiver concept where all the absorber tubes are on both the sides irradiated to the solar radiation. So there is a great potential to improve the thermal efficiency and reduce the material costs of the receiver compared to the External receiver [6].

2 Fundamentals

Concentrated solar power technology makes use of mirrors also known as heliostats, to focus a large amount of solar energy onto a small area where the heat absorption takes place, which is then transported to the steam turbine for the production of electricity. The most common concentrating technologies are Parabolic Trough collector, Linear Fresnel collector, Solar Dish or Stirling concept and Solar Tower plant. Both Parabolic trough collector and Linear Fresnel collector use the line focusing system where the reflectors track the Sun along one axis in contrast to Solar Dish and Tower plants, which use point focusing system in which heliostats track the sun bi-axially [1].

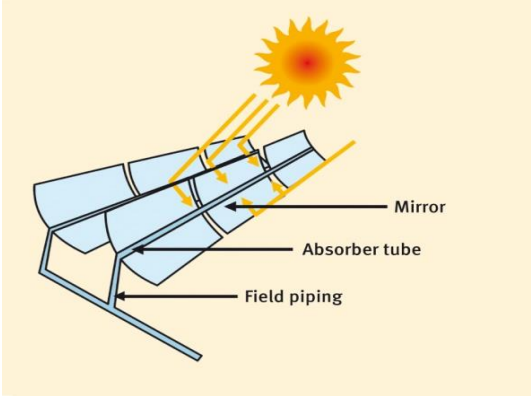

Figure 2: Parabolic Trough collector [7].

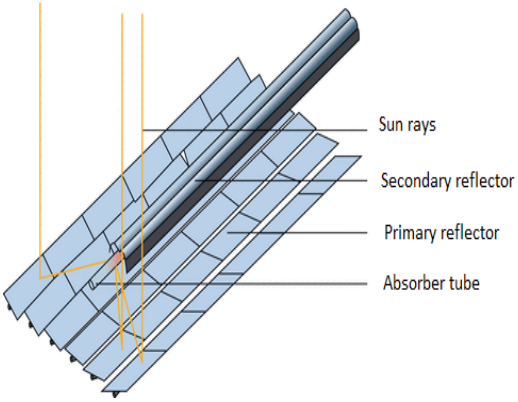

Figure 3: Linear Fresnel collector [7].

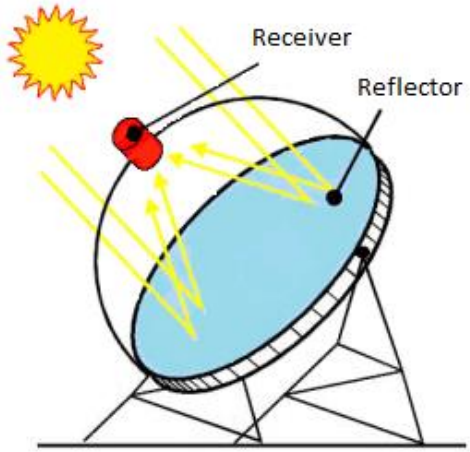

Figure 4: Solar Dish [7].

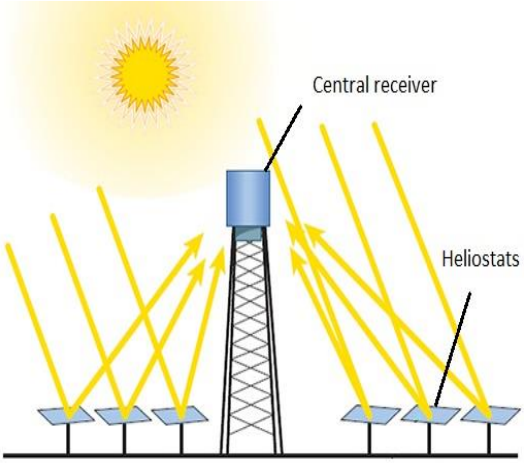

Figure 5: Solar Tower plant [7].

In Parabolic Trough collector, the mirrors which are parabolic in shape, are curved in one dimension to concentrate the solar energy onto an absorber tube which is mounted along its focal line [8]. In Linear fresnel collector, a group of reflectors that form a parabolic shape to reflect the solar radiation onto a downward-facing linear receiver as shown in Figure 3. In Solar Dish, the paraboloid mirror reflects the sunrays on to a focal point above the center of the dish whereas in Solar Tower

plant, a large field of heliostats concentrates the solar radiation on the receiver. Point focusing systems can achieve higher concentration ratios which allow the technology to operate at higher working temperature with higher efficiencies compared to Line focusing systems. The CSP technology's features such as cost, concentration ratio of the Sun and temperature range are listed below.

Type	Concentration ratio (Sun)	Temperature range (°C)	Thermo-dynamic efficiency	Relative cost
Trough	15-45	20-400	low	low
Fresnel	10-40	50-300	low	very low
Solar Dish	100-1000	120-1500	high	very high
Solar Tower	150-1500	300-2000	high	high

Table 1: Performance of CSP technologies [8], [1].

2.1 Solar Tower plant

Solar Tower plants are also known as Central Receiver Systems (CRS) employ a field of tracking heliostats that concentrate the solar irradiation onto the receiver, which is mounted on the top of a tower as shown in Figure 6. The absorber tubes placed in the receiver absorb the solar radiation and transfer the heat to the HTF i.e. nitrate salt, which enters absorber tubes at 290°C and after absorbing heat, exits at 565°C. Then the hot salt is sent into the hot storage tank, where the heat can be stored for several hours. Later the HTF is sent through the heat exchanger where it produces steam, which is further sent to the steam turbine to produce electricity. The stored heat can also be used for the production of electricity when there is no sunlight. Some of the central receivers with molten salts as a HTF are as shown below.

Project	Capacity	Location	Start year	Status
Solar Two	10 MW_{el}	USA	1996	closed
Gemasolar	19.9 MW_{el}	Spain	2011	operational
Crescent Dunes	110 MW_{el}	USA	2015	operational
NOOR III	150 MW_{el}	Morocco	2018	operational
SUPCON	50 MW_{el}	China	2018	operational
Atacama-1	110 MW_{el}	Chile	2018	under construction
Hami	50 MW_{el}	China	2019	operational
Tamarugal	450 MW_{el}	Chile	2021	under development

Table 2: Central receiver system with molten salt [8], [5], [9].

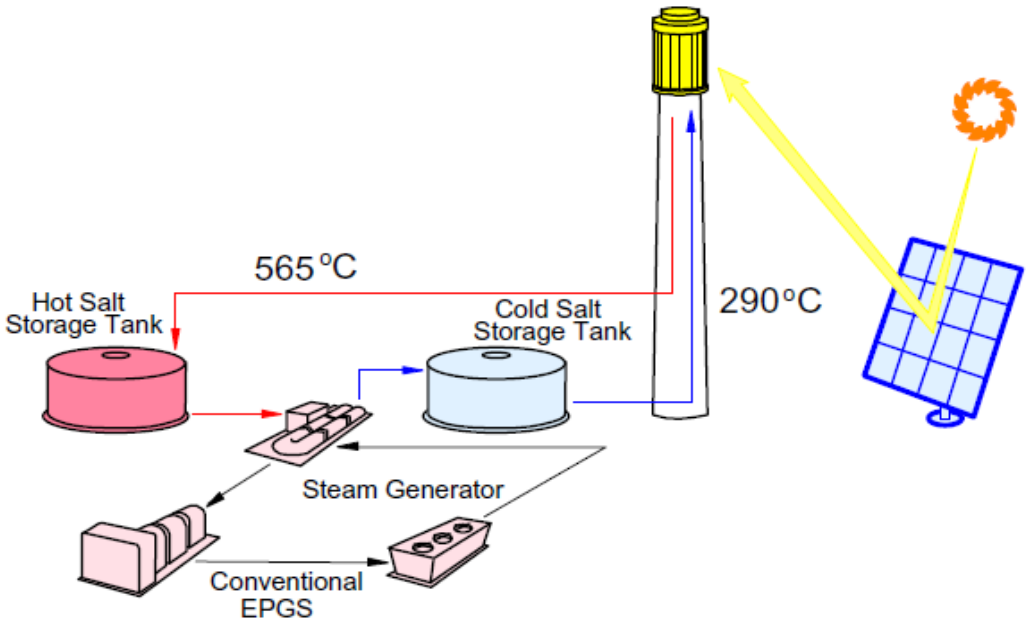

Figure 6: Schematic diagram of Solar plant **[10]**.

2.2 Heliostats (Collector system)

The primary function of the collector system is to concentrate solar radiation onto the receiver. The collector system consists of a field of heliostats around the receiver and tracking system to track the Sun and to focus energy on the receiver. In general, the solar radiation reflected by the heliostats acts as the input power on the receiver. The mirrors of the heliostats are flat or slightly concave placed on the pylons which are 10 m in height and each heliostat in CRS tracks the sun bi-axially [8]. During the day as the sun position changes, each heliostat must change its position with respect to the aiming point on the receiver. The surface area of heliostats range between 4-150 m^2 and is oriented individually to reflect the solar irradiation on the receiver [1]. The normal functioning of the heliostats takes place under 15 m/s wind velocity to avoid the damage [11]. For example, in the Crescent Dunes power plant, the receiver was mounted on 195 m tower surrounded by more than 10000 heliostats, each with 117 m^2 reflective area [5].

2.2.1 Heat flux

The main advantage of the heliostats field is that, it can focus a large amount of solar radiation 200-2000 kW/m^2 on the receiver [1]. Based on the aiming of heliostats, the amount of power incident, losses and heat flux densities on the receiver can be determined using raytracing software. A raytracing software known as SolTrace was first developed by National Renewable Energy Laboratory in the USA, to track the radiation incident on the receiver to determine the flux densities on the receiver [12]. The optical parameters such as the power reflected by heliostats, power received by the receiver surface and heat flux densities concentration on the receiver can also be obtained. The local salt temperature,

local salt velocities, heliostat aiming errors, insulation, material corrosion limits, field design and tube strains are the functions that limit the flux densities on the receiver surface [13]. The molten salt receivers can withstand flux densities up to 1 MW/m^2 [14].

2.3 Receiver System

2.3.1 Description

The receiver is one of the essential parts of the solar thermal plant because its performance affects the entire performance of the plant. The cost of energy obtained through the heliostats is relatively expensive, which provides economic incentives to improve the thermal efficiency of the receiver that enhances the plant's electricity production [13]. The receivers may be of different shape or size, but the main function of the receiver is to absorb the concentrated solar radiation incident on the absorber tubes and to transfer the heat to the HTF, which is flowing through it [15]. The HTF enters the receiver at 290°C and leaves out after passing through the series of panels of the absorber tubes to reach the desired outlet temperature of 565°C. The tower on which the receiver mounted will be around 75 - 200 m in height [1].

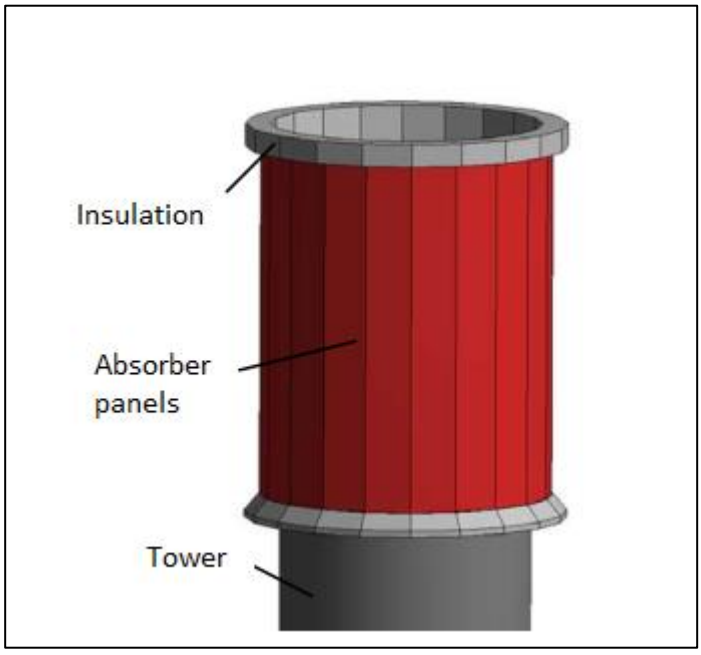

Figure 7: External tubular receiver [16].

2.3.2 Receiver concept

There are two types of tubular receiver concepts, External and Cavity receiver. In the External type receiver, the absorber surface is equal to the area which is exposed to solar radiation around the receiver, also known as aperture. The absorber tubes are oriented vertically around the support structure, which forms a cylindrical shape and the receiver can withstand heat flux densities up to 1

MW/m^2. The commercial receivers such as Gemasolar, Crescent dunes are examples of the External receiver. In the Cavity receiver, the absorber tubes are protected inside a cavity structure and the aperture of the receiver is either vertically or horizontally oriented. The difference compared to the External receiver is that the absorber tubes are arranged in a structure to protect from weather influences such as wind [17]. And the aperture size is less than the absorber surface, which reduces thermal losses such as radiation and convection losses to ambient because of a decrease in the area of the absorber surface but the design of the cavity receiver is complicated [6]. In the Cavity receiver, the peak heat flux densities can be increased because of smaller aperture opening to the absorber tubes. Themis receiver and Khi Solar One receiver are the examples of the Cavity receiver.

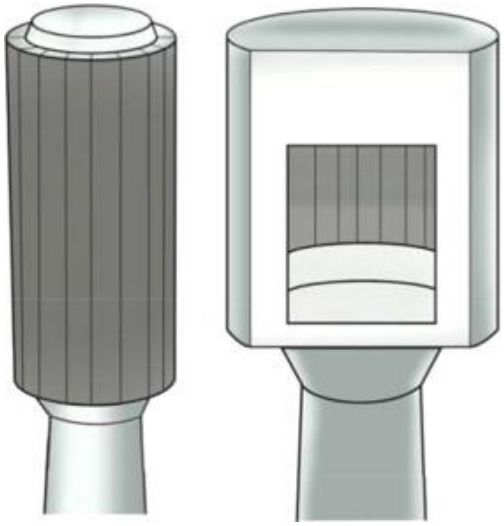

Figure 8: External receiver and Cavity receiver [6].

2.3.3 Receiver design

The design parameters of the receiver are the absorber tube diameter, the number of parallel and serial tubes in a panel, interconnection between the panels, total aperture area, geometric arrangement of absorber surface such as in External, Cavity receivers and maximum allowable flux densities of the receiver. Based on the above design parameters, Frantz et al. [3] developed a code called ASTRID, which can calculate different designs based on the applied boundary conditions such as inlet and outlet temperature, pressure drop and thermal power.

The External receiver consists of a large number of vertical blocks of tubes known as panels. The absorber panels in the receiver consists of inlet header, the inlet nozzles, the outlet nozzles, an outlet header and the tubes are individually supported at the top and bottom [18]. Each panel consisting of several tubes are arranged parallel and series to each other. For example, in Solar Two receiver there are 32 absorber tubes in each panel and in total there are 24 panels, which are arranged in series and parallel to each other [17]. The HTF flows in serpentine

with respect to each panel in the receiver. The arrangement of tubes and panels are shown below in Figure 9. In the External receiver, the entire area of the absorber portion is exposed to the sunrays. Hence the thermal losses are high, whereas in the Cavity receiver the absorber area is surrounded by the cavity to minimize the thermal losses [5].

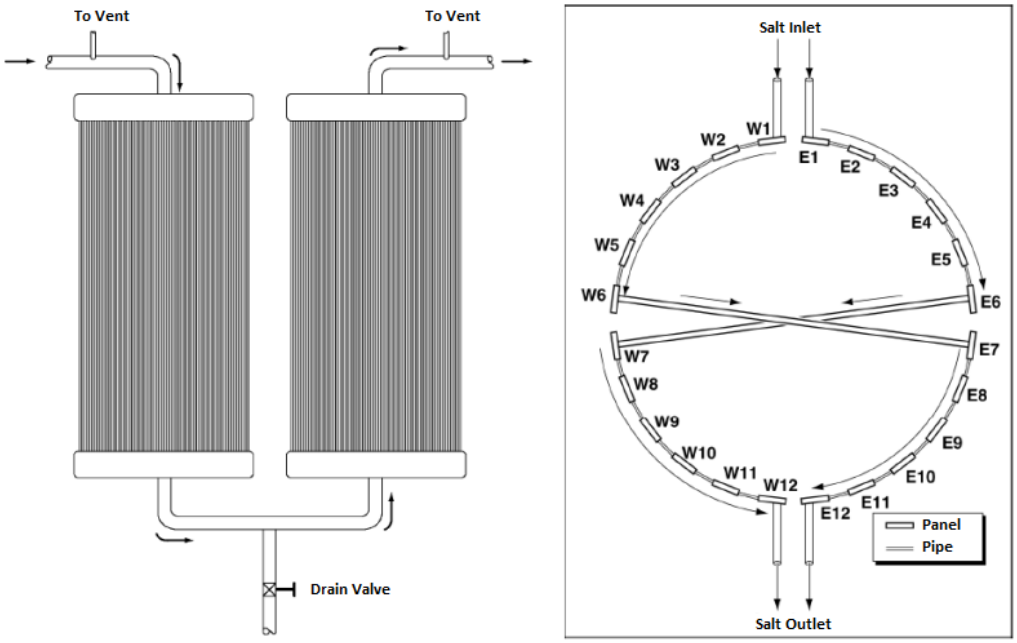

Figure 9: Solar Two receiver arrangement [17].

2.3.4 New geometries of receiver

Nowadays most of the commercial Solar Tower plants use the external cylindrical tubular receiver concept where the absorber tubes are irradiated only on one side, so the other side of the tubes does not involve directly with the heat transfer. Due to this, higher thermal stress on the tubes can be experienced and restricts the allowable flux densities [19]. So, the Fractal like geometries [20] are introduced where either side of the tubes are solar irradiated. These geometries improve the efficiency of the receiver which reduces the thermal losses due to its light-trapping properties.

The hat-like geometry structures was used to reduce the radiative and convective losses from the top of the receiver as shown in Figure 10. Usually, the receiver coating can maintain solar absorptance up to 0.95 but the coating does not last for a longer period [20]. If the coating degrades below 0.9, the Fractal geometries can improve the absorptance significantly. Results showed that the radiative losses were reduced due to low view factors at the hot interior area of the receiver because the interior regions are too narrow, so most of the emitted radiation gets trapped and absorbed between the neighboring surfaces.

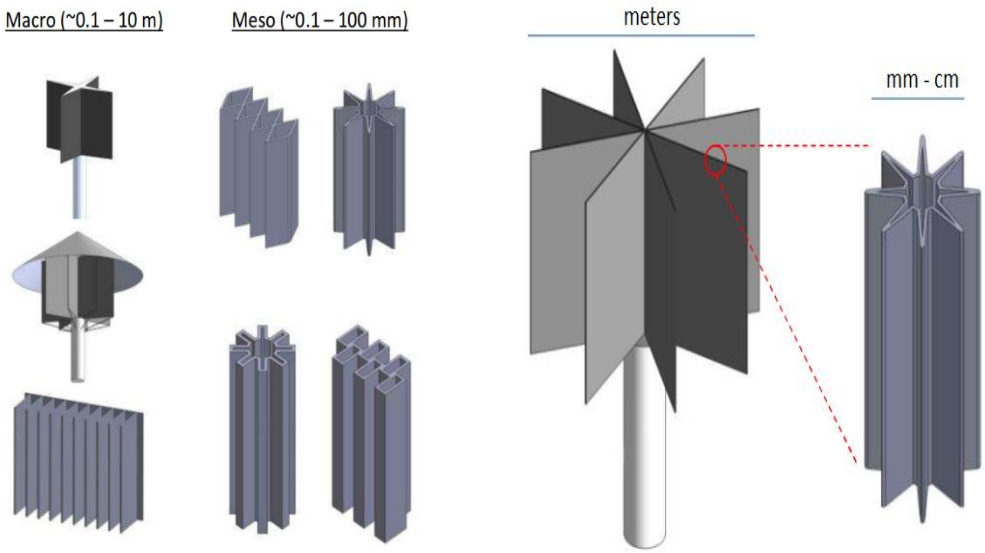

Figure 10: Receiver designs for macro and meso [20].

2.3.5 Star receiver

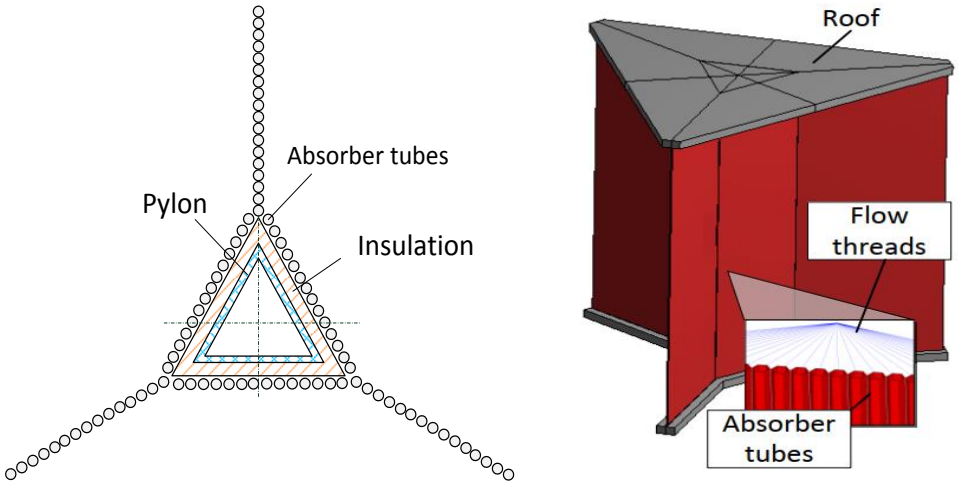

Figure 11: Star receiver with a central pylon [6].

In the Star receiver with a central pylon, the absorber tubes are arranged along the three cantilevers which are inclined at 120° to each other which depicts the star shape and the structure is supported by a central pylon. The absorber tubes are staggered to provide better stability to the structure. The mass flow in the absorber tubes is serpentine flow with respect to each panel in the receiver and the tubes are vertically suspended as in the External receiver. The absorber tubes around the center pylon are irradiated on one side because the other side of the tubes is covered by thermal insulation as shown in Figure 11. But absorber tubes in each cantilever are irradiated on either side, this in turn doubles the output of each absorber tube in the Star receiver compared to the External receiver, where

only one side of the absorber panels is irradiated. And also the material cost of the receiver can be reduced around 36 % in comparison to the External receiver [6]. The overall cost of the Star receiver with pylon is less expensive than the External receiver. The thermal analysis of the Star receiver with 140 MW_{th} was carried out in high performance molten salt project. The reflection losses in the Star receiver are 5 % and thermal efficiency was improved by 1 % in contrast to the External receiver, but the radiation and convection losses are more [6].

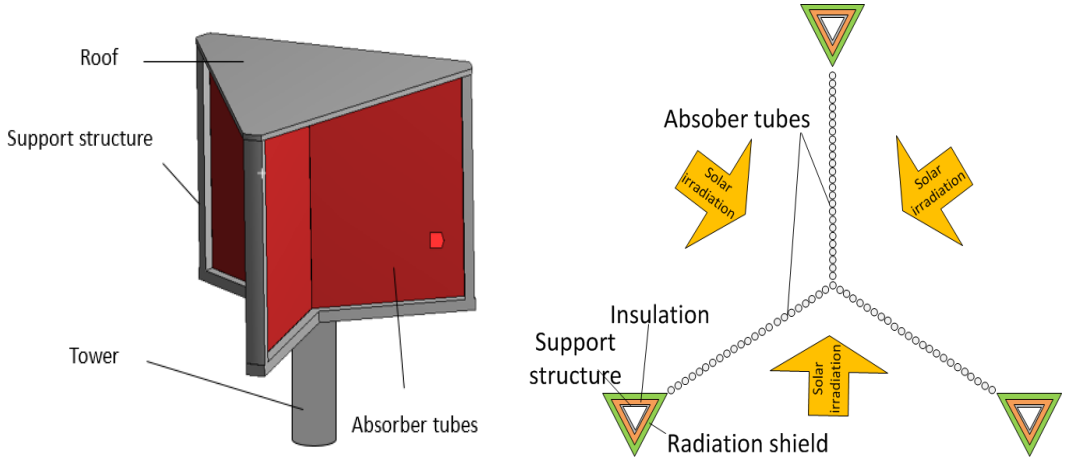

Figure 12: Star receiver.

In the Star receiver without a central pylon, the absorber tubes are arranged along the three cantilevers which are oriented at 120° to each other. The pylons support the tubes at the end of each cantilever and the roof structure as shown in Figure 12. The arrangement of the tubes and mass flow direction is same as the Star receiver with a central pylon. Here all the absorber tubes in the receiver are irradiated on either side, this in turn doubles the flux densities on each tube with the same flux density as that of External receiver. The aperture size of the Star receiver is slightly smaller than the External receiver, but the installed absorbing area can be drastically reduced because more power can be absorbed with less number of absorber tubes. Due to the cavity effect, the optical losses can be reduced and the thermal performance of the Star receiver can be improved [6]. H is the irradiated length of the absorber tubes and r as shown in Figure 13.

	External	**Star**
Aperture area	$2 \cdot \pi \cdot r \cdot H$ $\approx 6.28 \cdot r \cdot H$	$3 \cdot \sqrt{3} \cdot r \cdot H$ $\approx 5.2 \cdot r \cdot H$
Projected absorber area	$2 \cdot \pi \cdot r \cdot H$ $\approx 6.28 \cdot r \cdot H$	$2 \cdot 3 \cdot r \cdot H$ $\approx 6 \cdot r \cdot H$
Installed absorber area	$2 \cdot \pi \cdot r \cdot H$ $\approx 6.28 \cdot r \cdot H$	$3 \cdot r \cdot H$

Table 3: Absorber area in Star receiver [6].

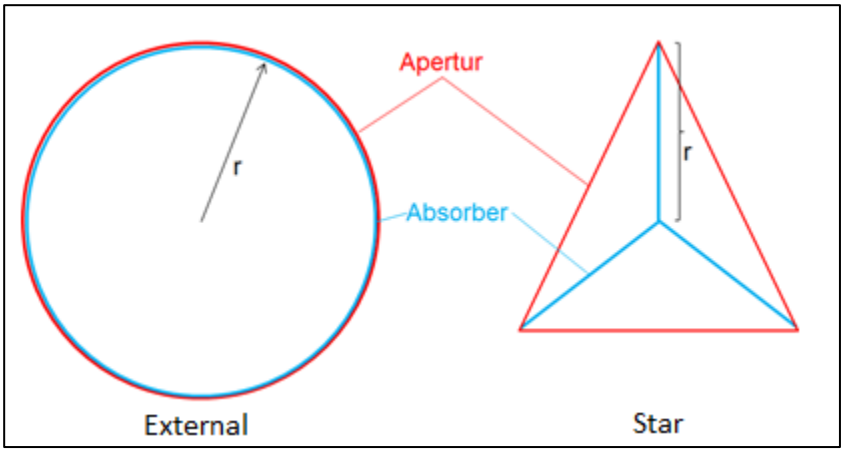

Figure 13: Area of External and Star receiver [6].

2.3.6 Receiver efficiency

The thermo-optical efficiency of the receiver is the ratio of the power absorbed by the salt to the power entering the receiver aperture when each heliostat assigned specific targets on the receiver. Pacheco et al. demonstrated [21], the receiver efficiency was measured using power on method. According to this method, the inlet and outlet temperatures of salt are constant under the steady-state condition, the wind velocities and the temperature distribution on the receiver surface are independent of incident power level. Therefore, the thermal losses are independent of incident power [21] because the convective and radiative losses are the function of the receiver surface temperature.

$$\eta_{\text{thermo-optical}} = \frac{P_{\text{entering aperture, aiming}} - P_{\text{ref\_amb}} - P_{\text{conv\_amb}} - P_{\text{IR\_amb}}}{P_{\text{entering aperture, aiming}}}$$

$$\eta_{\text{thermo-optical}} = \frac{P_{\text{abs, salt}}}{P_{\text{entering aperture, aiming}}} \quad (1)$$

Where $P_{\text{entering aperture, aiming}}$ is the amount of solar radiation incident on the receiver surface, $P_{\text{ref\_amb}}$ is the amount of solar radiation reflected to the atmosphere, which is based on the geometry arrangement in the receiver and material absorptance in the solar spectrum. The other losses such as convection ($P_{\text{conv\_amb}}$) and radiation ($P_{\text{IR\_amb}}$) losses to ambient are dependent on the surface temperature and area of solar irradiated surface. $P_{\text{abs, salt}}$ is the power absorbed by the salt flowing through the absorber tubes.

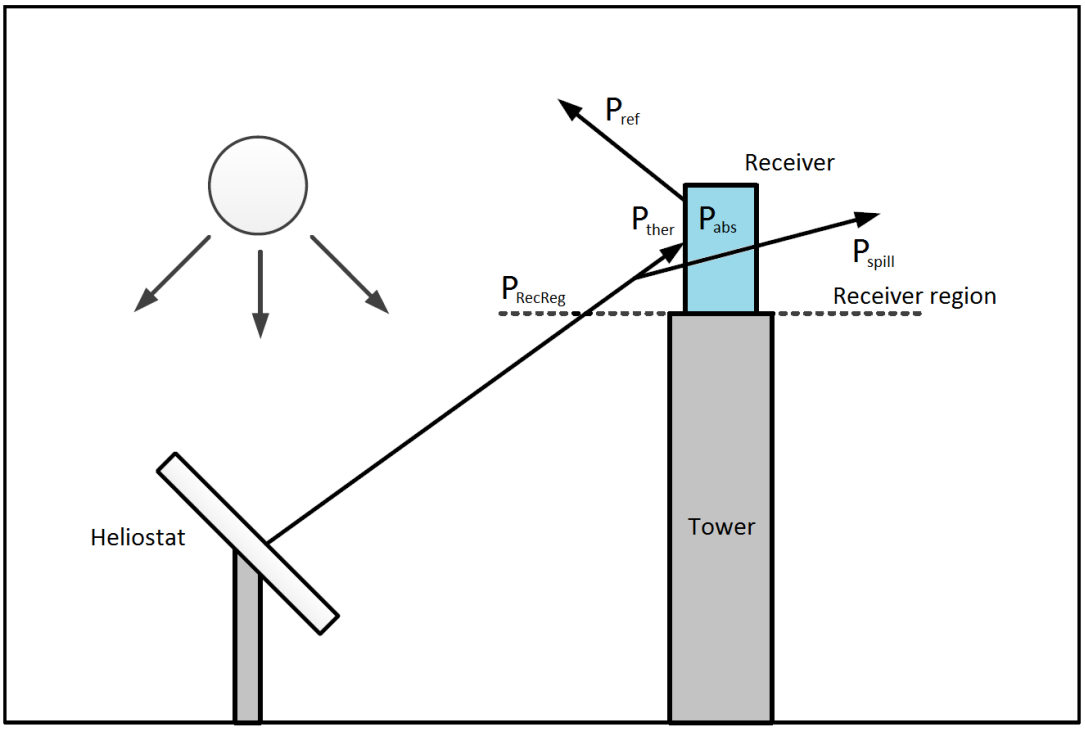

Figure 14: Losses in the receiver [22].

The amount of power reaching the receiver region from the heliostats after atmospheric absorption is P_{RecReg} and P_{spill} is some part of the power reaching the receiver region but does not hit the receiver. P_{ref} and P_{ther} are the power losses on the absorber surface to the atmosphere due to reflection and thermal losses such as convection and radiation. P_{abs} is the amount of power absorbed by the salt.

The overall thermo-optical efficiency of the receiver is the ratio of power absorbed by the salt to the power reaching the receiver region.

$$\eta_{\text{overall thermo-optical}} = \frac{P_{RecReg} - P_{spill} - P_{ref} - P_{ther}}{P_{RecReg}} \quad (2)$$

2.4 Material

The solar radiation incident on the receiver is first absorbed by the opaque solid called absorber tube, and then the heat is exchanged between the absorber tubes and HTF. Therefore the absorber tube also limits the maximum operating temperature, based on its material properties [15]. In order to improve the absorptivity of the absorber tubes in the receiver, black Pyromark is painted on the tube but this coating degrades over a time period due to higher operating temperature [23]. For example, in Solar Two receiver, the absorber material was 316H stainless steel and the surface of the tubes was painted with black Pyromark to absorb 95% of the incident radiation on it [21]. However, nickel-based alloys are

preferred over stainless steel such as Inconel 625 and Hastelloy 230 were also suitable for the receivers operating above 700 °C due to its corrosion resistance property [24].

2.5 Heat Transfer Fluid (HTF)

The main characteristics required for the solar HTF are high thermal stability, high thermal conductivity, high working temperature and high specific heat capacity that help during thermal storage of HTF [25]. The high thermal stability of HTF allows operating with a low melting point to avoid freezing and higher working temperature. The nitrate salt is the mixture of 60 % Sodium nitrate ($NaNO_3$) and 40 % potassium nitrate (KNO_3), which is popularly known as Solar Salt. The first plant to use Solar Salt as HTF was Molten Salt Electric Experiment with 5MW power in Albuquerque in 1985 [26]. The drawback of nitrate salts is a high melting point, which is 240°C so it is important to maintain temperature of the salt above the melting point to avoid freezing in the absorber tubes and it is thermally stable up to 600°C [21]. And the receiver is preheated by focusing a few heliostats before filling salt to avoid plugging inside the tubes [14]. When water/steam is used as HTF, the steam coming out of the receiver can be sent directly to the steam turbine for the production of electricity, whereas for other HTF's steam is generated through a heat exchanger before sending into the turbine [27]. The disadvantage of steam as a HTF is an uneconomical storage medium because the energy must be transferred to other medium such as oil, but it results in substantial energy losses while transferring one medium to the other and cannot operate at high temperature due to its instability [25].

The nitrate salts have an adequate heat capacity which is advantageous for heat storage. And most of the central receiver plants use Solar Salt as a HTF because they are widely available and are inexpensive [5]. Even though the central receivers are capable of operating at higher solar flux, but the heat transfer fluid limits the operating temperature of the receiver [5]. Table 4 shows the temperature limits of the heat transfer media.

Heat transfer medium	Peak flux (kW/m^2)	Outlet temperature (°C)
Water / Steam	~ 600	390-560
Molten nitrate salt	~ 1000	~ 600
Liquid sodium	~ 2500	~ 800
Ceramic particles (direct heating)	~ 3000	> 1000

Table 4: Peak flux and outlet temperature of heat transfer media [5].

3 Theoretical background

The energy that is transferred through the boundary of a thermodynamic system due to the temperature difference between the system and the surrounding is known as heat. There are three modes of heat transfer conduction, convection and radiation.

3.1 Heat conduction

Heat transfer takes place due to molecular interaction in a medium such as solids, liquids and gases. Due to this molecular collision, transfer of energy takes from the molecules at higher kinetic energy to the molecules at lower kinetic energy [28]. The heat conduction is defined with Fourier's law as

$$\dot{Q} = -\lambda A \frac{dt}{dx} \tag{3}$$

Where λ = Thermal conductivity (W/m K)
A = Area (m^2)
$\frac{dt}{dx}$ = Temperature gradient (K/m)

3.2 Heat convection

Heat transfer takes place due to the bulk motion of the fluid. Newton's law of heating defines the heat convection as [28]

$$\dot{Q} = \alpha A (T_W - T_f) \tag{4}$$

Where α = Convective heat transfer coefficient (W/(m^2 K))
A = Area (m^2)
T_w = Temperature of the wall (K)
T_f = Temperature of the fluid (K)

3.3 Heat radiation

The heat emitted in the form of electromagnetic radiation by any matter with a temperature greater than absolute zero to its surrounding is known as heat radiation. The radiation emitted by a body is given by [28]

$$\dot{Q} = \sigma \varepsilon A T^4 \tag{5}$$

Where σ = Stephan's Boltzmann constant ($5.67*10^{-8}$ W/(m^2 K^4))
ε = Emissivity of the body (-)

A = Area (m^2)
T = Temperature of the body (K)

3.3.1 View factor

The radiation exchange between the surfaces can be determined using the view factor. View factor is a parameter which is purely dependent on the orientation of the geometry that accounts for radiation losses between the surfaces [28]. If two surface i and j of area A_i and A_j face each other at distance R with an angle θ_i and θ_j, then the view factor (F_{ij}) can be determined using the formula below.

$$F_{ij} = \frac{1}{A_i} \int_{A_i} \int_{A_j} \frac{\cos\theta_i \cos\theta_j}{\pi R^2} \, dA_i \, dA_j \tag{6}$$

Then the radiation losses between the surfaces in the model can be approximated analytically by

$$\dot{Q}_{ij} = \sigma \varepsilon F_{ij} A T^4 \tag{7}$$

3.4 Finite Element Method (FEM)

The finite element method is a numerical method that determines approximate solutions, which is being used for numerous engineering applications such as structural, fluid flow, heat transfer and electro-magnetic analysis. In the modern engineering world, it is difficult to determine exact analytical solutions due to the complexity of geometry and boundary conditions [29]. So, the solutions are approximated using Finite element analysis. FEM discretizes large models into a number of smaller domains known as finite elements and these elements are connected by nodes. Depending on the number of nodes, the elements are categorized into different ordered elements (first order, second order, etc.). The main aim of the FEM is to find nodal solutions corresponding to nodal loads. In thermal analysis, the primary nodal variable is temperature. The discrete FEM renders the global equation system as shown below.

$$[\lambda][\theta] = [q] \tag{8}$$

Where [λ] is the thermal conductivity matrix, $[\theta]$ is the vector of unknown nodal temperature and [q] is the vector of nodal loads. The system is subjected to Dirichlet boundary condition to prescribe nodal temperatures $[\theta]$, where these are known**.** An external heat flux on the boundary of the domain e.g. solar radiation, is applied by means of Neumann boundary condition, which contribute to [q].

3.5 Raytracing

The solar radiation concentrated on the receiver can be modeled using ray tracing. The local flux densities on the receiver are found numerically by using the Monte Carlo method [12] which calculates based on the statistical computation of rays reflected from the source to the receiver. Raytracing is a technique used to track the path of solar radiation incident on the receiver surface, which was reflected by heliostats. The flux densities on the receiver surface can be predicated using raytracing software called SPRAY which was developed by DLR (German Aerospace Center) [30].

4 Thermo-optical model of the STAR receiver

The main aim of this thermo-optical model is to determine the temperature distribution of the salt in the receiver, peak heat flux required to reach 565 °C as outlet salt temperature, maximum surface temperature on the receiver, thermal losses, solar absorptance and thermo-optical efficiency of the receiver.

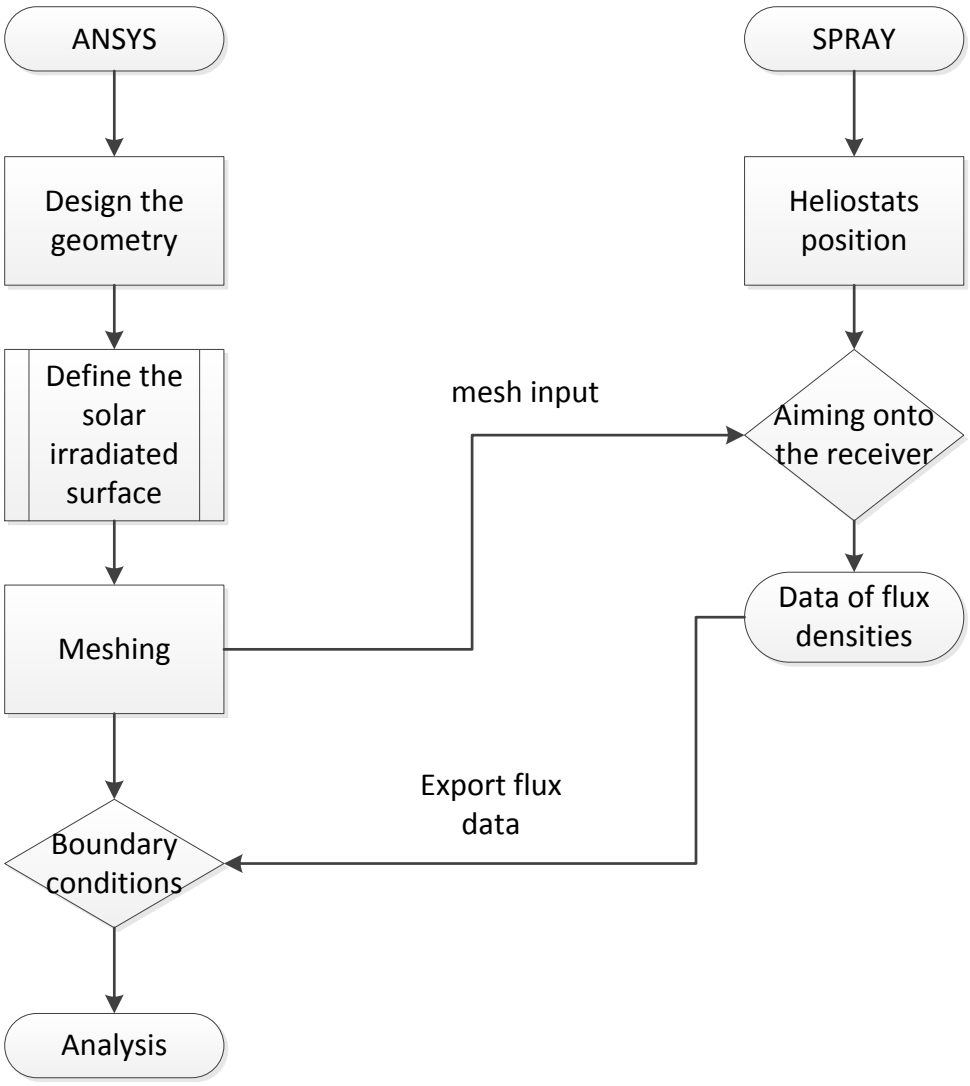

Figure 15: Data Flow for the analysis.

The Finite Element Analysis (FEA) is carried out in ANSYS software using “Steady-State Thermal” analysis. Raytracing is carried out in SPRAY software to obtain the heat flux densities on the receiver surface. The details of the model and boundary conditions applied in ANSYS and SPRAY are described in the following sections. After designing the geometry of the receiver, the outer surface of the absorber panels which is exposed to solar radiation must be defined. Then the meshing is carried on the complete geometry and the input mesh file generated will be given

as the input in the SPRAY software, where the heliostats are aimed on the receiver. Based on the aiming of the heliostat field, flux densities on the receiver surface are generated. This heat flux data is imported as external data in ANSYS workbench, and further analysis is carried out.

4.1 Receiver configuration

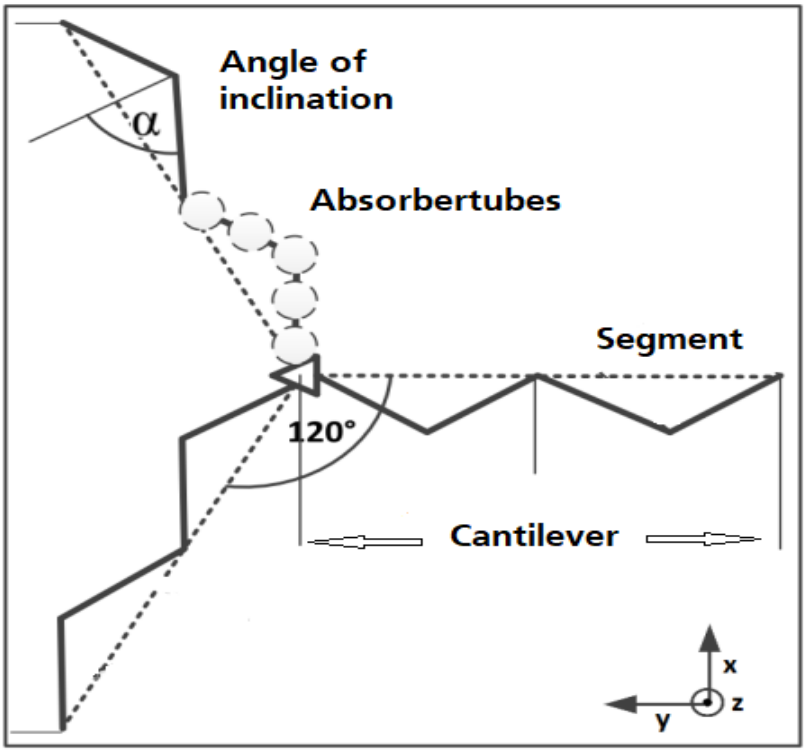

Figure 16: Orientation of Star receiver.

The Star receiver consists of three cantilevers facing each other at 120°. Each cantilever consists of a large number of absorber tubes arranged in the form of segments and panels. The absorber tubes are arranged vertically in all the absorber modules. A segment consists of 21 tubes with one tube at the center of the segment and remaining tubes are inclined at 50° with respect to the center tube on either side, each with ten tubes. The fins are arranged between the absorber tubes to provide better stability under wind loads.

The cantilever A and B consist of five panels arranged in series to each other as shown in Figure 17, where each panel consists of two segments. The cantilever C in the southern direction consists of three panels, with four segments in each panel. The irradiated length of each absorber tube in the receiver is 15.75 m and the thermal capacity of this Star receiver is 560 MW_{th}.

Thermal performance	**560 MW_{th}**	
Number of cantilevers	3	
Each segment	21 tubes	
Cantilever A and B	5 panels	
Each panel	2 segments	
Cantilever C	3 panels	
Each panel	4 segments	
Inner diameter of the tube	50	mm
Outer diameter of the tube	56	mm
Distance b/w each tube (fins)	2	mm
Length of each tube	15.75	m
Total number of tubes	672	-
Alpha (α)	50	°

Table 5: Geometry details.

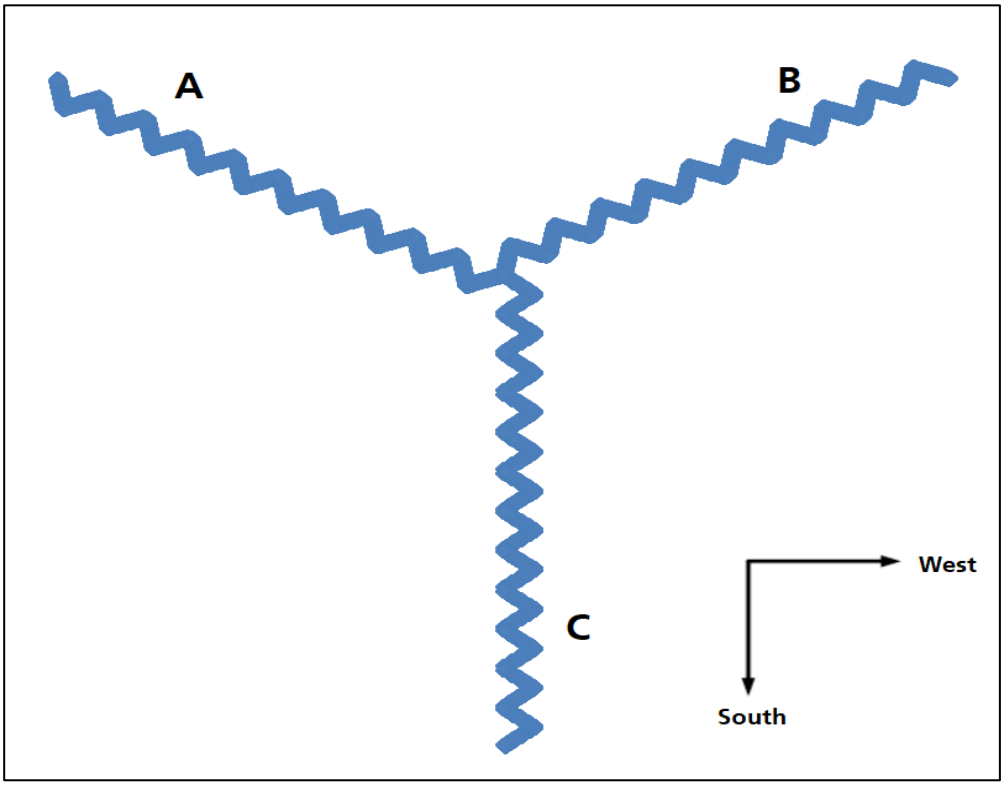

Figure 17: Star receiver.

4.2 Raytracing (Optical model)

The local heat flux densities on the outer surface of the absorber tubes are obtained by radiation tracking using software known as SPRAY. For Star receiver, Crescent Dunes heliostat field is considered to have a better comparison with the External receiver performance. The cantilever A and B are facing towards pole because more number of heliostats will be available to concentrate solar radiation on the receiver as shown in Figure 18, so the peak flux densities will be on cantilever A and B.

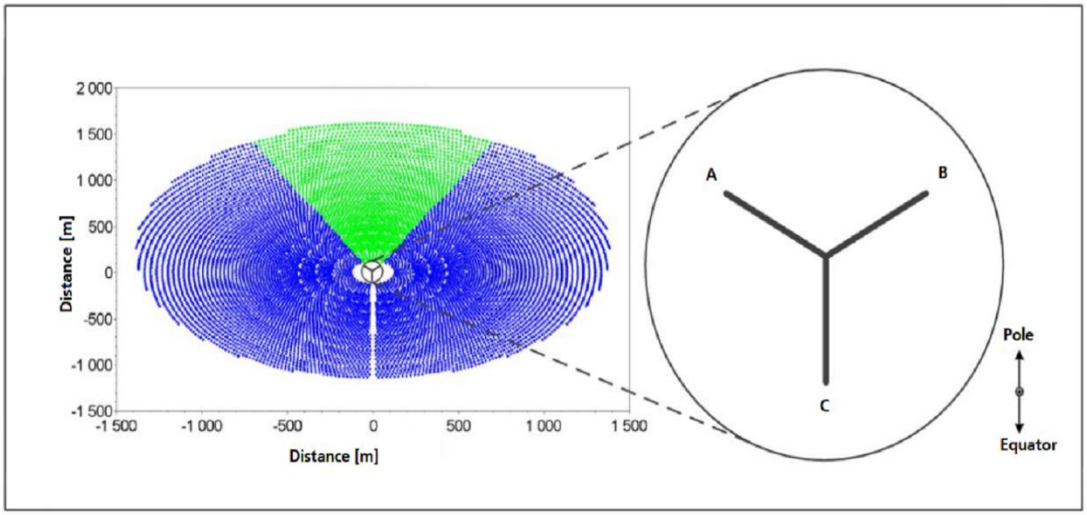

Figure 18: Heliostats distribution around the Star receiver [22].

The allowable flux densities on cantilever A and B will be more than cantilever C because of the lower salt temperature. By using meshed geometry as the input data from the FEM model, SPRAY calculates the local heat flux densities on each panel of the receiver based on the aiming of the heliostats. When all the heliostats are aimed only on the center of the receiver to focus the solar radiation, results in high heat flux densities (2- 3 MW/m^2) which limits the heat transfer medium because the salt becomes unstable above 600 °C. Therefore, the aiming points of heliostats are distributed on the complete receiver, so the peak flux densities are reduced on the receiver. The obtained heat flux data can be imported on the receiver surface as heat flux boundary condition for the analysis. Figure 26 indicates the obtained flux data on the receiver surface. The heat flux densities on the receiver are further scaled in ANSYS to reach the desired outlet temperature of the salt to 565 °C.

4.3 Thermal FEM model

The boundary conditions are applied to define the flow of heat in the body. The boundary conditions are applied as shown below in Figure 19. T_{w_in} and T_{w_out} are the temperatures of the inner and outer walls of the absorber tube. Q_{Solar} is the amount of solar radiation absorbed by the absorber tubes from the heliostat field.

T_{salt} is the temperature of the nitrate salts in the absorber tube and T_{amb} is the ambient temperature around the receiver. The amount of heat lost from the tube to the surroundings through convection and radiation is shown as Q_{Conv_amb} and Q_{Rad_amb} respectively. Q_{Conv} is the heat transferred to the nitrate salts through heat convection.

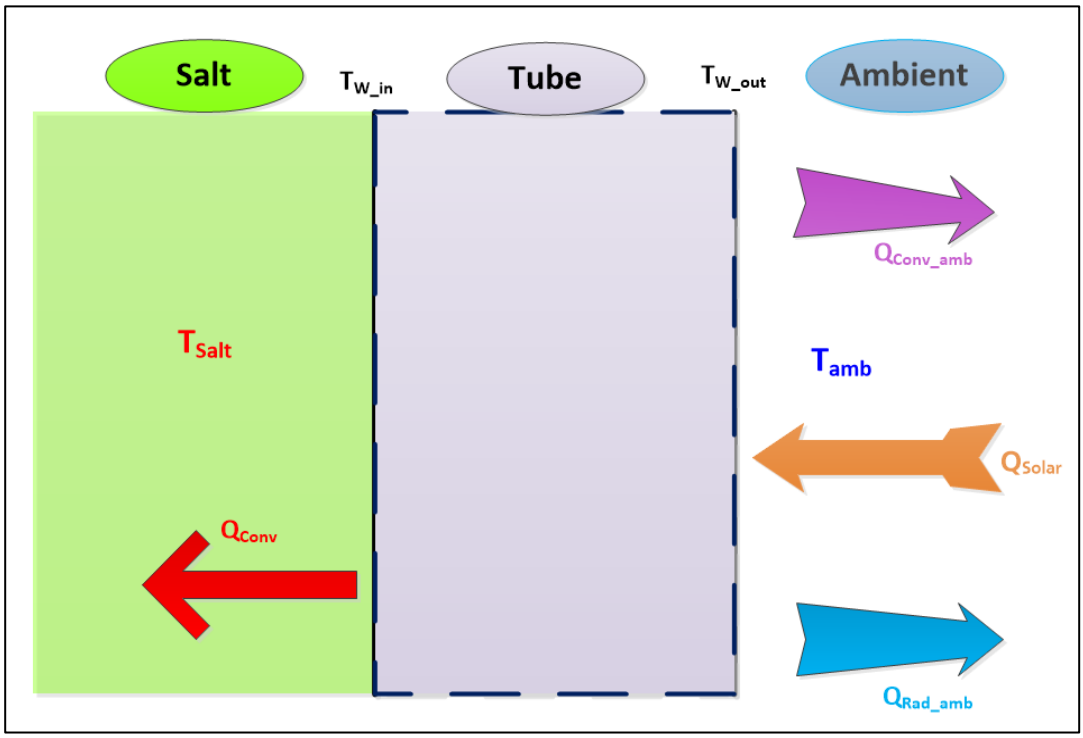

Figure 19: Schematic representation of boundary conditions.

4.3.1 Material properties

The material used in this project is Nickel-Chromium-Cobalt-Molybdenum alloy, which is also known as Inconel Alloy 617 can withstand to high temperature and have oxidation resistance up to 1800 °F [31] with the thermal conductivity of 21.5 W/(m K). The material properties can be defined in the engineering data of the workbench model. The material properties account for the amount of heat absorbed by the heat transfer fluid flowing through the tubes.

Material	Alloy 617	-
Thermal conductivity	21.5	W/(m K)
Density	8000	kg/m^3
Thickness of absorber tubes	3	mm

Table 6: Material details.

4.3.2 Convection to ambient

The heat lost from the outer surface of the receiver to the surrounding

environment is defined by convection boundary condition as shown in Figure 21. This boundary condition is applied with a film coefficient of 8.4 W/(m² K) at ambient temperature 30 °C on the outer surface of the absorber tubes. The film coefficient is calculated based on wind velocity around the absorber tubes. Usually heliostats are operated up to 15 m/s wind speed measured at 10 m in height due to their design stability [11]. So, the receivers are not operated under high wind velocities. Based on the wind velocity around the heliostats, the velocity around the receiver can be determined by

$$v_{wind,\ R} = 0.19 \cdot \left(\frac{z_{Kat}}{0.05}\right)^{0.07} \cdot \ln\left(\frac{H_{Tower}}{z_{Kat}}\right) \cdot c_0 \cdot v_{wind,\ H} \tag{9}$$

$$= 19\ \mathrm{m/s}$$

Where
z_{Kat} = 0.05 according to DIN EN 1991-1-4 Kat 2
c_0 = 1 according to DIN EN 1991-1 Standard value
$v_{wind,\ H}$ = Wind velocity around heliostats at 10 m height
H_{Tower} = Height of the receiver tower (180 m)

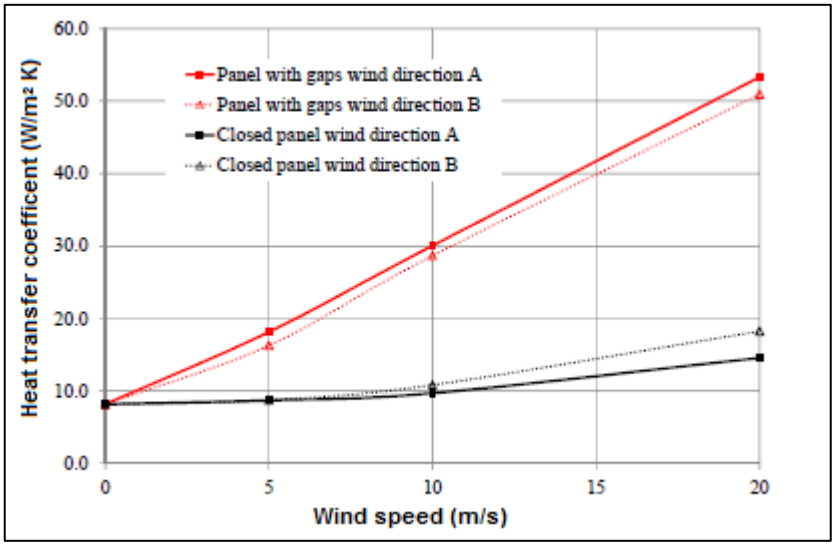

Figure 20: Heat transfer coefficient as a function of wind speed [19].

So the heat transfer coefficients are 8.4 W/(m² K) and 18.3 W/(m² K) corresponding to 0 m/s and 20 m/s wind velocity around the receiver with the fins in between the absorber tubes and 53.4 W/(m² K) at 20 m/s without the fins, which are obtained from the study carried out by Uhlig et al. [19]. The convection to the ambient boundary condition is applied on the outer surface of the absorber tubes in the receiver.

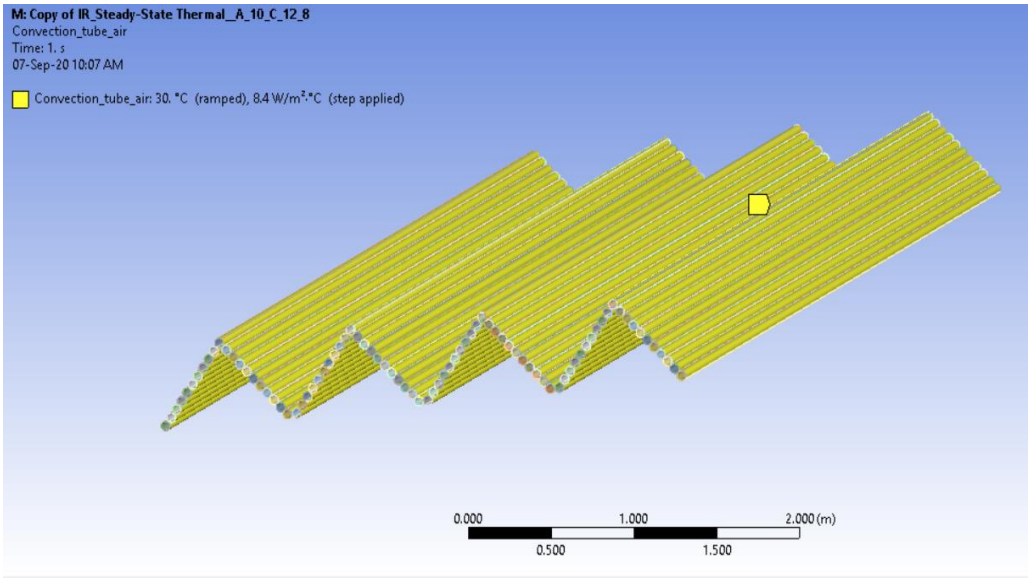

Figure 21: Convection to ambient.

4.3.3 Radiation to ambient

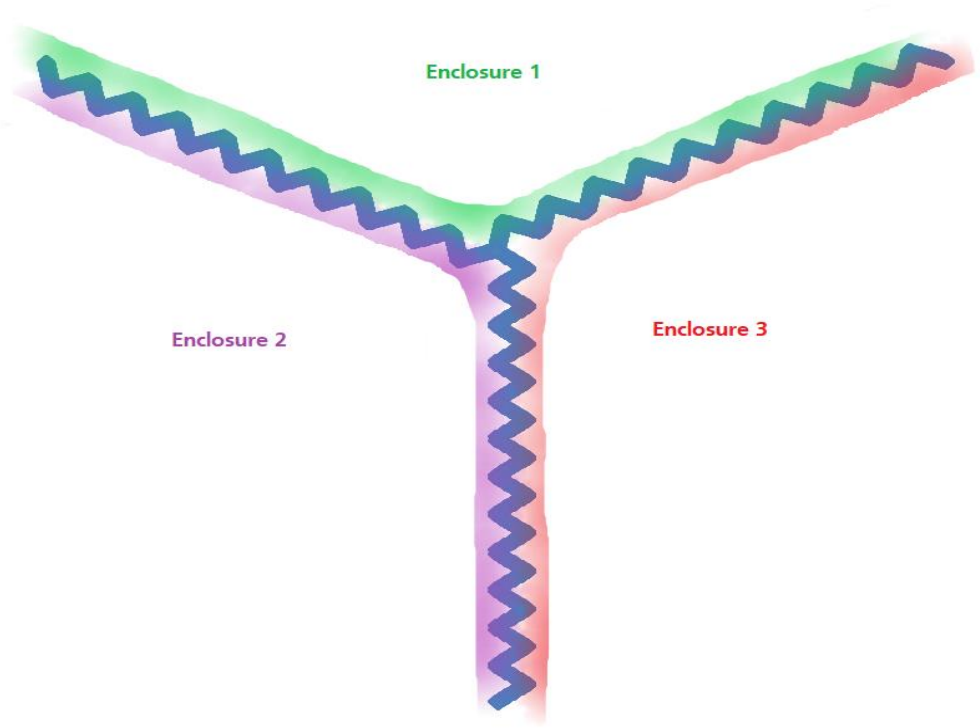

Figure 22: Radiation boundary condition.

Usually absorber tubes are coated with black Pyromark paint which has a thermal emissivity of 0.83 [21]. In the Star receiver, due to its geometry orientation most of the radiation gets trapped in between the segments. Some part of the radiation emitted by the absorber tubes are reflected and absorbed by the neighboring tubes. The heat exchange between the absorber tubes and the atmosphere is defined with radiation boundary condition which is applied on the outer surface of

the tubes with an emissivity of 0.83 at ambient temperature 30 °C. As there are three enclosures as shown in Figure 22, for each enclosure, the surface to surface radiation boundary condition is applied. ANSYS calculates the amount of heat exchanged between the surfaces in each enclosure and the heat lost from the absorber surface to the environment.

4.3.4 Mass flow

In the current model, flow threads are modeled using line bodies inside the absorber tubes, through which the mass flow rate can be defined during the analysis. The molten nitrate salt is employed as the heat transfer fluid, which is a mixture of 60 % sodium nitrate ($NaNO_3$) and 40 % potassium nitrate (KNO_3). The thermal conductivity and specific heat capacity of the nitrate salt are 0.4 W/(m K) and 1463 J/(kg K), respectively. The mass flow of the nitrate salt enters at 290 °C from the center of the receiver and flows as shown in Figure 23. The input of nitrate salts is given to the first panel of the cantilever in eastern (A) and western direction (B) from the center of the receiver. The mass flow in the absorber tubes takes place in a serpentine flow with respect to each panel, but the flow direction of all tubes in each panel will be parallel to each other. At the end of fifth panel in both the cantilevers (A and B), the salt flow converges and flows into the third cantilever in the southern direction from the center of the receiver.

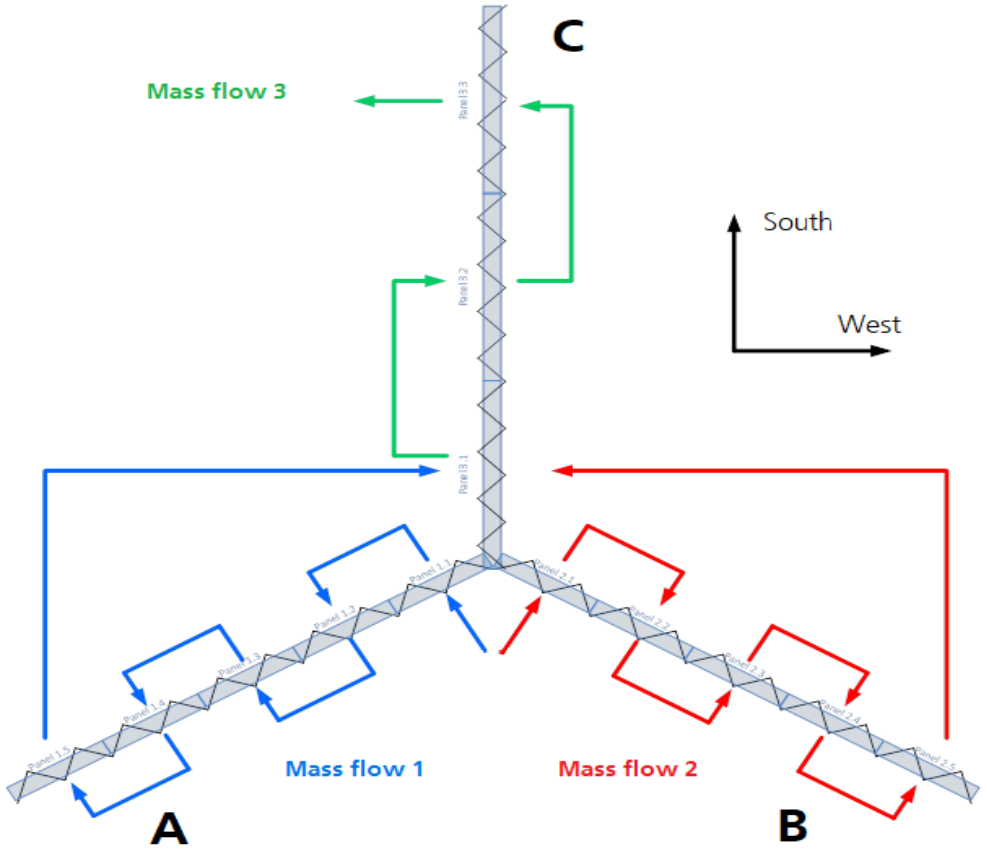

Figure 23: Mass flow in Star receiver.

In general, heat transfer fluid must pass through five series panels in cantilever A and B, in order to pass on through the remaining three series panels in the cantilever C to reach the desired outlet temperature. The mass flow rate of the complete receiver is 1391 kg/s. The mass flow rate input is given to flow threads in the first panel of the cantilever A and B. Each panel consists of two segments which has 48 tubes, therefore the mass flow input is given to 84 tubes of the receiver with 16.55 kg/s for each tube.

$$\dot{Q} = \dot{m}\, C_p\, (T_{S,\ out} - T_{S,\ in}) \tag{10}$$

$$\dot{m} = \frac{\dot{Q}}{C_p\, (T_{S,\ out} - T_{S,\ in})} \tag{11}$$

$$= 1391\ \mathrm{kg/s}$$

When the sun is at its peak (during afternoon), the heliostats reflecting solar radiation on the receiver surface will be at its peak, so that the receiver can be operated at maximum capacity (560 MW) also known as full load condition. During full load condition, the mass flow rate will be constant for the entire receiver and the heat flux can be scaled (increase or decrease) to reach 565 °C as the desired outlet temperature of the salt. During sunrise, sunset or cloudy conditions, the solar radiation reflected by the heliostats will decrease, this condition is known as part-load. During part-load conditions, to maintain the constant outlet temperature of the salt at 565 °C, the mass flow input must be reduced.

Total Mass flow rate	1391	kg/s
Cantilevers	A & B	
Panel	1	
Segments	2	
Each segment	21 tubes	
Mass flow input	84 tubes	
Specific heat capacity of the salt (C_p)	1464	J/(kg K)
Thermal performance ($\dot{Q}$)	560	MW
Inlet temperature of the salt ($T_{S,\ in}$)	290	°C
Outlet temperature of the salt ($T_{S,\ out}$)	560	°C
Thermal conductivity of the salt	0.473	W/(m K)

Table 7: Input of mass flow.

4.3.5 Convection to the HTF

The convection to the HTF is applied, to define the fluid temperature over the length of the tube. The convection to the salt is implemented by importing heat transfer coefficients along the length of the tubes in each panel. The heat transfer coefficient is evaluated with respect to each panel length by using Gnielinski correlation [7] as shown in chapter 4.3.5.3. The heat transfer coefficients are calculated using the formulas below.

$$\alpha = \frac{N_u \lambda}{L} \tag{12}$$

Where N_u = Nusselt number (-)
λ = Thermal conductivity of the fluid (W/m K)
L = Characteristic length (m)

4.3.5.1 Velocity of HTF

The velocity of the HTF changes along the length of the tube due to change in density and viscosity. As the HTF passes through the absorber tubes in each panel, the temperature of the HTF rises, so the density of the fluid and viscosity between the fluid and tubes surface decreases. The temperature of HTF is assumed to rise linearly along the length of the tube. Based on this assumption, the velocity of HTF along the tube length in each panel is calculated.

$$u = \frac{\dot{m}}{\rho A} \tag{13}$$

Where $\dot{m}$ = Mass flow rate (kg/s)
ρ = Density of HTF (kg/m^3)
A = Cross-sectional area of the tube (m^2)

4.3.5.2 Reynolds number

Reynolds number used to predict the flow pattern of the HTF with respect to different flow velocities in the absorber tubes. The flow tends to be laminar with a low Reynolds number and at higher values (>10^4) the fluid flow is turbulent [32]. The obtained results through the analytical approach are greater than 10^4, so the fluid flow through the absorber tubes will be turbulent. Reynolds number is calculated as

$$Re = \frac{u D_i}{v} \tag{14}$$

Where u = Flow velocity of HTF (m/s)
D_i = Inner diameter of the tube (m)
v = Kinematic viscosity (m^2/s)

4.3.5.3 Nusselt number

When the fluid flow is turbulent ($Re>10^4$), Gnielinski [32] deduced an equation for the heat transfer during the flow of liquids through a tube as

$$Nu = \frac{(\xi/8)\ Re\ Pr}{1 + 12.7\ \sqrt[2]{\xi/8}\ (Pr^{2/3} - 1)} \left[1 + \ (D_i/l)^{2/3}\right] \tag{15}$$

$$\xi = (1.8\ \log_{10} Re - 1.5)^{-2} \tag{16}$$

Where
- Re = Reynolds number (-)
- Pr = Prandtl number (-)
- D_i = Inner diameter of the tube (m)
- L = Length of the tube (m)

With the linear interpolation of the fluid flow temperature with respect to the overall length of the absorber tube to reach the desired output flow temperature are determined. These interpolated temperatures are used as local temperature of the fluid along the length of the tube and the heat transfer coefficients of the fluid are obtained through Nusselt number. The graph below shows the obtained results of heat transfer coefficients and temperature along the length of the absorber tubes by the above analytical method.

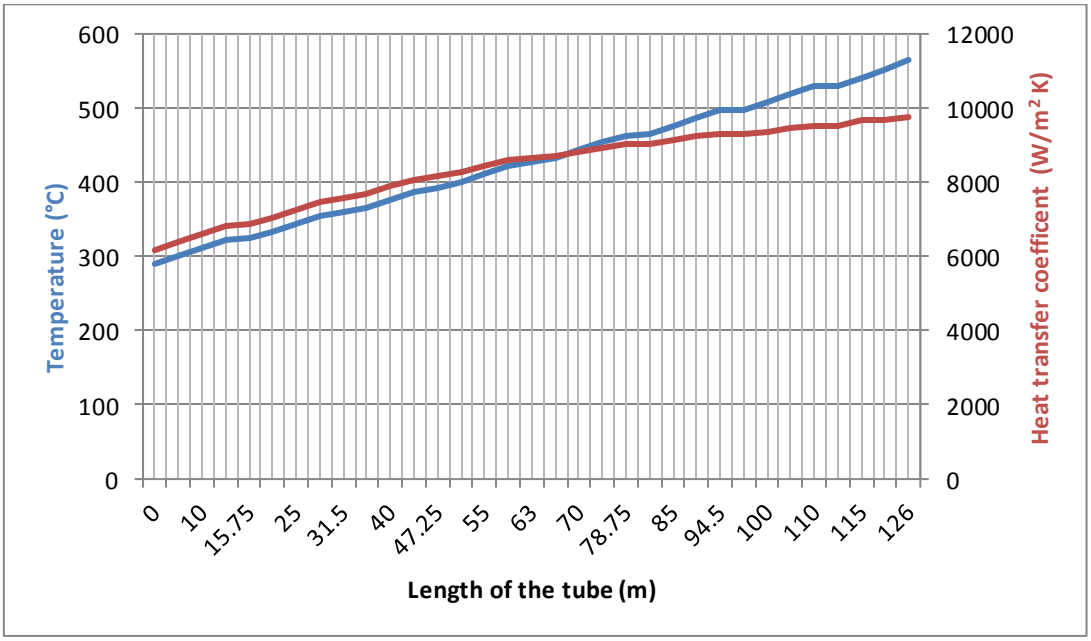

Figure 24: Heat transfer coefficients along the length.

The determined heat transfer coefficients along the length of the tubes are imported on to the inner surface of the absorber tubes in ANSYS as shown in Figure 25.

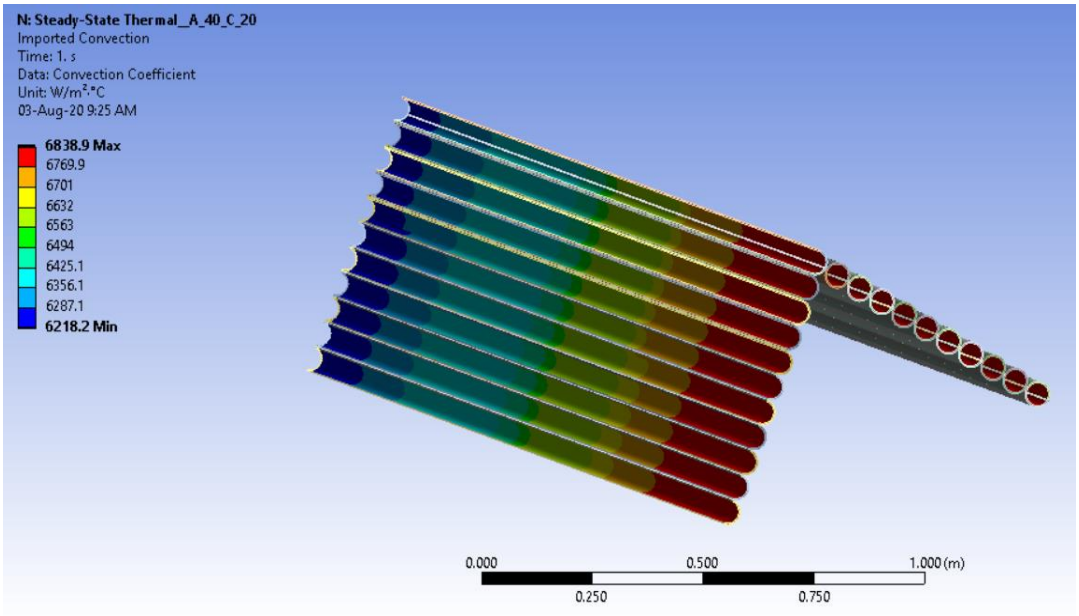

Figure 25: Convection to salt.

4.4 Heat flux

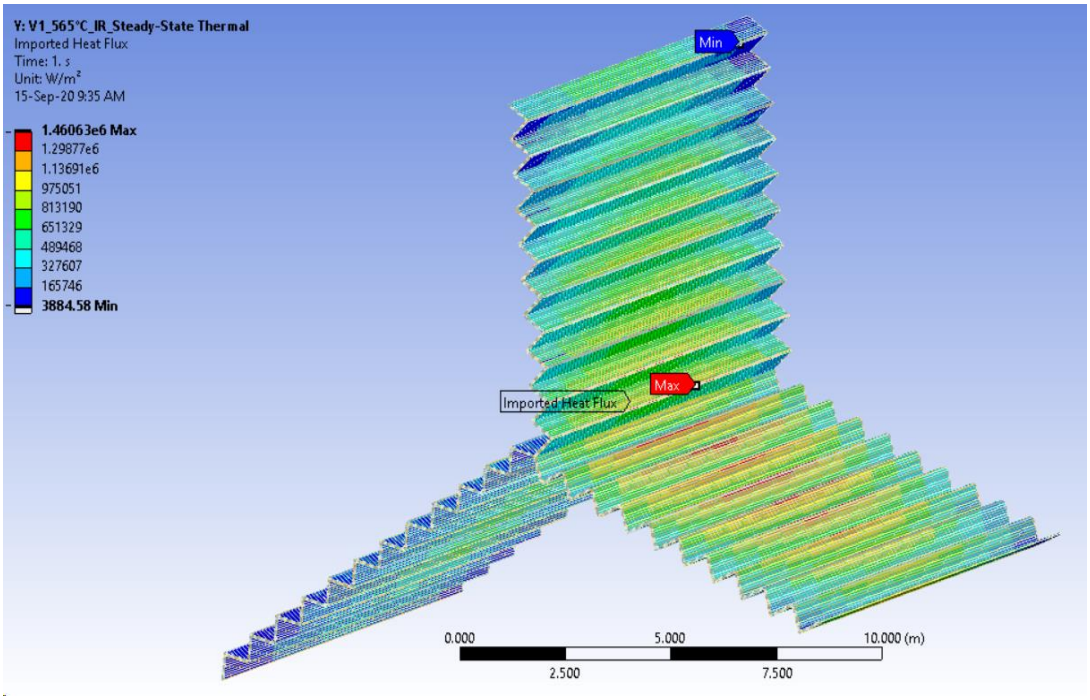

Figure 26: Heat flux on the Absorber panels.

The total solar energy incident on the absorber surface per unit area is known as heat flux which is indicated as Q_{solar} in Figure 19. In the model, this boundary condition is applied as heat flux on the outer surface of the absorber tubes as shown in Figure 26. When the heliostats aiming are spread on the complete

receiver, a peak heat flux density of 1.46 MW/m^2 is required to reach the desired outlet temperature and the mean flux densities on the Star receiver is 0.34 MW/m^2. The obtained peak flux densities are high, so the heliostats aiming on the receiver must be optimized in the future projects. The flux data obtained through the raytracing method can be imported on the complete receiver panels. On full load condition, the mass flow rate in the receiver will be constant. If the outlet temperature of nitrate salts 565 °C is not reached, then the heat flux must be scaled to reach 565°C as outlet temperature of nitrate salt. During the part-load condition, the local heat flux densities on the receiver surface will decrease. so, the mass flow rate in the receiver is reduced in such a way that the outlet temperature of the salt is 565 °C.

4.5 Summary of assumptions

1. The inlet (290 °C) and outlet (565 °C) temperature of the HTF are constant with an accuracy of ±2 °C.
2. The temperature of the HTF will rise linearly in the absorber tubes of each panel in the receiver.
3. The infrared emission from the surface of the absorber tubes is 0.83.
4. The ambient temperature around the receiver is 30 °C.

5 Quality control

5.1 Mesh study

The main goal of the mesh study is to obtain a mesh independent solution. The mesh study can be carried out by varying the number of elements in the axial and circumferential direction of the tube. The element types in the model are hexahedral and prism elements. In the first case, the elements along the axial direction of the tube are varied and with the elements along the circumferential direction are kept constant (minimum number of elements). The mesh convergence is reached with 20 elements along the axial direction of the tube, and the thermo-optical efficiency of the model is 92.05 % with the radiation enclosures. The difference in the efficiency between the basic and fine mesh is around 0.03 %. In the second case, the elements along the circumferential direction of the tube are varied and with elements along the axial direction are kept constant (minimum number of elements). The mesh convergence is reached with a minimum number of elements along the circumferential direction of the tube and the efficiency of the receiver is 92.01 % with the radiation enclosures, but the calculation time was more because of smaller element size. Hence the efficiency is independent of the elements along the circumferential direction. To obtain 565 °C as the outlet temperature of the molten salt, a peak flux of 1.46 $\mathrm{MW/m^2}$ is required for this Star receiver.

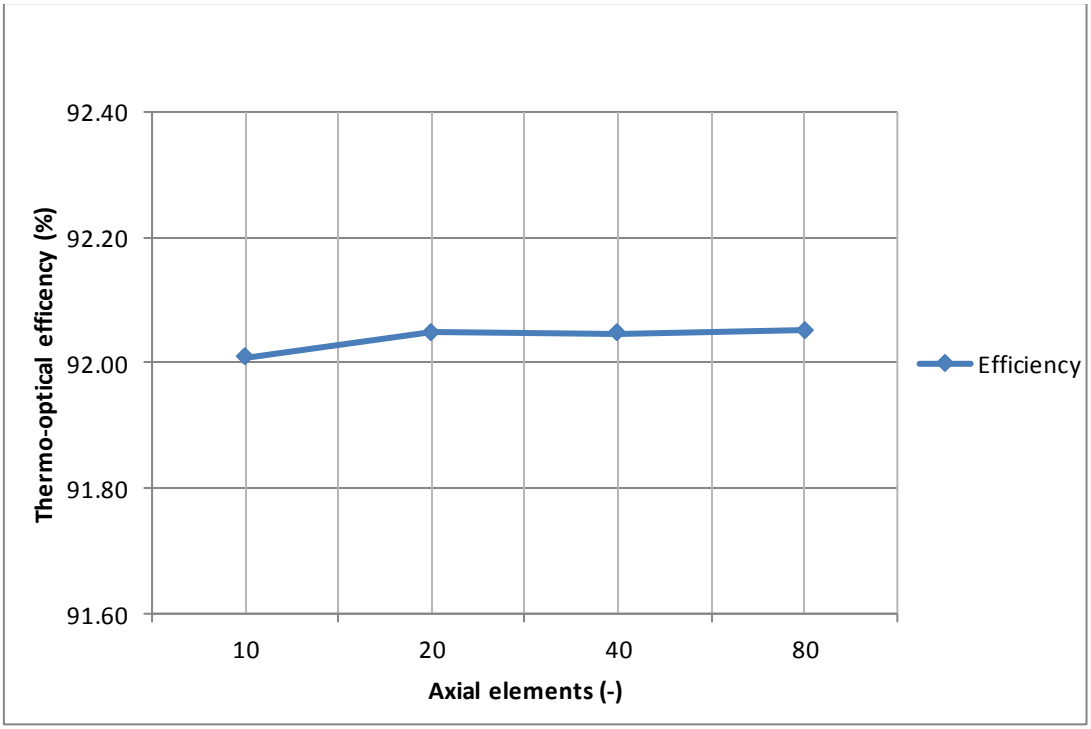

Figure 27: Mesh study.

5.1.1 Temperature

The maximum temperature on the outer surface of the absorber tubes is 832 °C with fine mesh and 820 °C with the basic mesh. The temperature is also converged with 20 axial elements along the tube. The maximum surface temperature on the receiver is high mainly due to high peak flux densities which must be optimized in future projects. So, that the receiver surface temperature will be reduced.

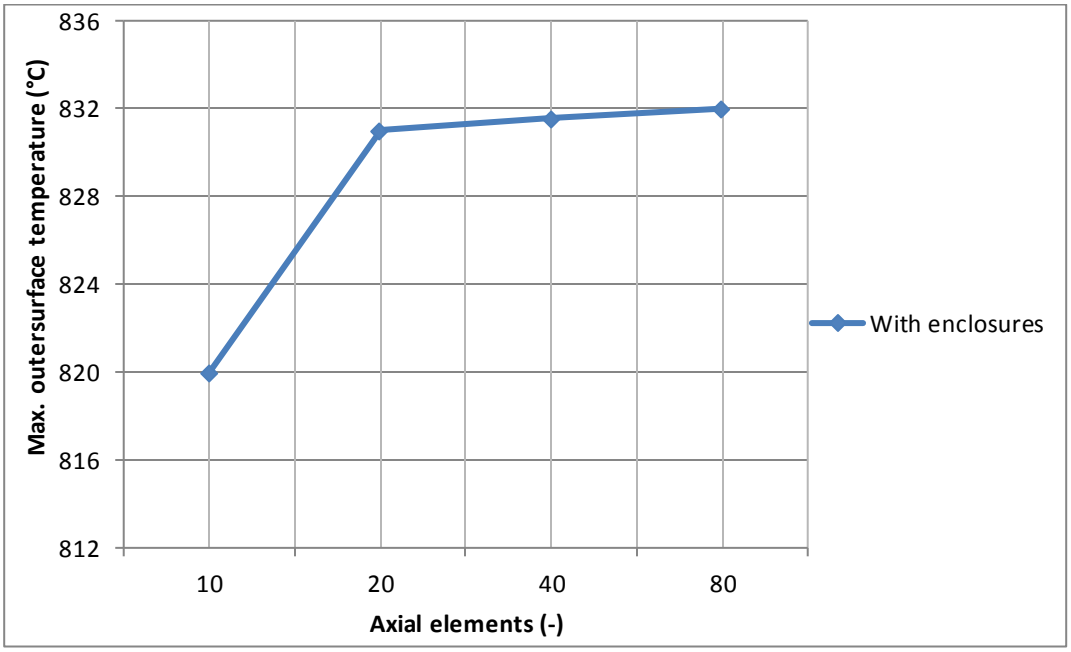

Figure 28: Maximum temperature on the absorber tubes.

5.2 Analytical results

The thermal losses in the receiver are calculated analytically to validate the results obtained through the analysis in ANSYS.

5.2.1 View factor

View factor is a parameter which is purely dependent on the orientation of the geometry that accounts for radiation losses between the surfaces of a segment. In the current model, the local view factor for a segment is determined as shown in Figure 29. Here A and B are absorber surfaces and C is an open surface to atmosphere through which emitted radiation will be lost.

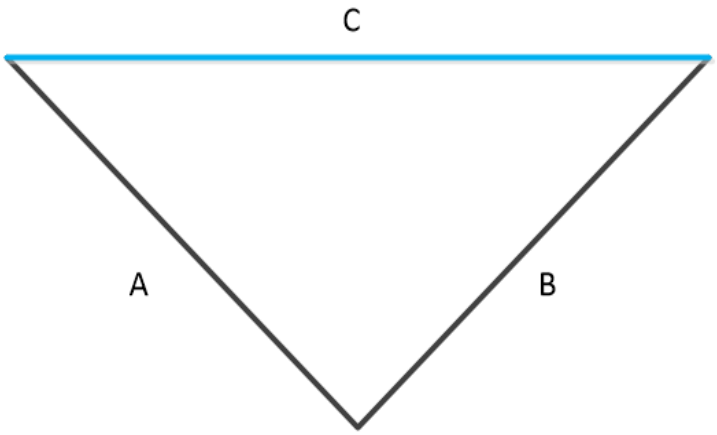

Figure 29: View factor.

The view factor for three-sided enclosure [28] can be calculated as

$$F_{A-C} = \frac{L_A + L_C - L_B}{2L_A} \tag{17}$$

Length of surface A (L_A)	0.588	m
Length of surface B (L_B)	0.588	m
Length of surface C (L_C)	0.9	m
View factor from (A+B) to C	0.766	-
View factor from A to B	0.234	-
View factor from C to A	0.5	-
View factor from C to B	0.5	-

Table 8: View factor details.

The view factor from B to C is same as the view factor from A to C because the length of A and B are equal. So, the view factor of the segment (A+B) to ambient (C) is 0.766 which indicates around 24 % of the emitted radiation is again absorbed by the absorber tubes.

5.2.2 Thermal losses

The radiation and convection losses to ambient are determined analytically based on the surface temperature obtained through the analysis in the ANSYS software. The thermal losses are calculated analytically based on the mean surface temperature of the receiver using formulae in chapter 3. The mean surface temperature of the receiver is assumed to be 486 °C, obtained from the thermal

analysis. The analytically obtained radiation and convection losses are 21.2 and 6.96 MW, respectively. The numerical results obtained from ANSYS are 17.5 MW radiation losses and 7.63 MW convection losses, which are close to the analytical results. An error of 20 % and 6 % are observed in radiation and convection losses between the results shown in Table 9. The error difference is more in radiation losses due to the assumed mean temperature and radiation losses are directly proportional to the fourth power of the temperature.

	Analytical (MW)	**Numerical (MW)**
Radiation losses to ambient	21.2	17.5
Convection losses to ambient	6.96	7.63

Table 9: Comparison of thermal losses.

6 Results

6.1 Results of the optical simulation

6.1.1 Intercept efficiency

Intercept efficiency is the ratio of power incident on the receiver aperture to the power reaching the receiver region. The amount of solar radiation reaching receiver region will be more than the amount of radiation reaching the aperture of the receiver because some parts of the radiation account for spillage losses which is calculated to be around 14.6 %. The spillage losses in Star receiver are quite high due to complex geometry compare to the External receiver that accounts for 3-5 % of spillage. The spillage losses can be reduced by optimizing the heliostats aiming on the receiver surface. The intercept efficiency of the Star receiver is 85.4 %.

$$\text{Intercept efficiency} = \frac{P_{\text{incident on receiver aperture}}}{P_{\text{RecReg}}} \tag{18}$$

Power reaching the receiver region	712	MW
Power entering the receiver aperture	608	MW
Spillage losses	104	MW
Intercept efficiency	85.4	%

Table 10: Intercept efficiency.

6.1.2 Solar absorptance

Absorptivity is a property that determines the amount of solar irradiation absorbed by the receiver surface. The absorptivity of the Star receiver is determined using the SPRAY result, which shows the heat absorption of the receiver as shown below. In total, 96 % of solar radiation incident on the receiver will be absorbed by the absorber tubes and the remaining 4 % lost due to reflection of the absorber tubes. The solar absorptance in the External receiver is around 93 %, so the absorptance in the Star receiver is improved by 3 % because of geometry configuration where the solar rays get reflected multiple times and absorbed between the neighboring tube surfaces before escaping to the atmosphere. Therefore, the absolute absorptivity (α_{abs}) of the Star receiver is 96 %.

$$\alpha_{abs} = \frac{P_{\text{absorbed by the absorber tubes}}}{P_{\text{incident on receiver aperture}}} \tag{19}$$

Power incident on the receiver aperture	608	MW
Power absorbed by the receiver	584	MW
Absolute absorptivity	96	%

Table 11: Solar absorptance.

6.1.3 Aiming efficiency

Aiming efficiency is the ratio of the power entering the receiver aperture with the aim points spread on all the absorber modules to the power entering the aperture when all heliostats are aiming at the center of the receiver. The aiming efficiency of the Star receiver is 93.6 %. When the heliostats are aimed at the center, peak heat flux densities on the receiver reach to 6 MW/m^2 compared to 1.46 MW/m^2 when aiming is spread on complete receiver. Aiming at different areas of the receiver is done with the target point assignment for each heliostat. So, each heliostat is assigned a target point on the receiver to reduce the peak flux densities, else excess solar radiation on the receiver limits the material and the HTF. In case of the External receiver, the aiming efficiency is 96.5 % so the heliostats aiming need to be further optimized to improve the aiming efficiency of the Star receiver.

$$\eta_{\text{aim}} = \frac{P_{\text{entering aperture, aiming}}}{P_{\text{entering aperture, no aiming}}} \tag{20}$$

Power incident on receiver aperture without the aiming	649	MW
Power incident on the receiver aperture with the aiming	608	MW
Aiming efficiency	93.7	%

Table 12: Aiming efficiency.

6.2 Results of the thermal simulation

The analysis of the Star receiver model is carried out after applying all the boundary conditions. A peak heat flux of 1.46 MW/m^2 is required to reach the desired outlet temperature of 565 °C. The graph below indicates the inlet temperature of the salt in each absorber tubes panel of the receiver and the temperature rise is almost linear in the receiver which makes a good initial assumption. The temperature rise is steep in the starting panels which is due to higher flux densities. After passing through the first five series panels in the cantilever A and B, the salt temperature is 468 °C before converging the mass flows to enter on to the panel 6 in the cantilever C. Then passing on to the panel 7

and 8, the outlet temperature of the salt at the end of panel 8 is 565 °C. The rise in temperature of the salt on passing through the series of absorber panels is indicated in flow threads temperature in the receiver is as shown in Figure 31.

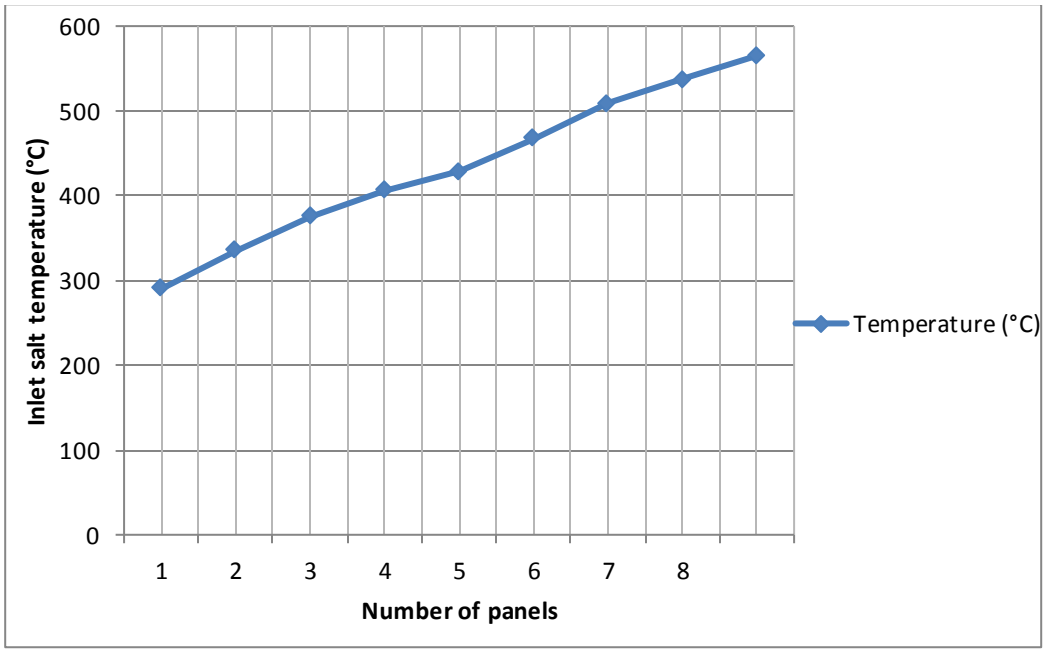

Figure 30: Inlet salt temperature of each panel.

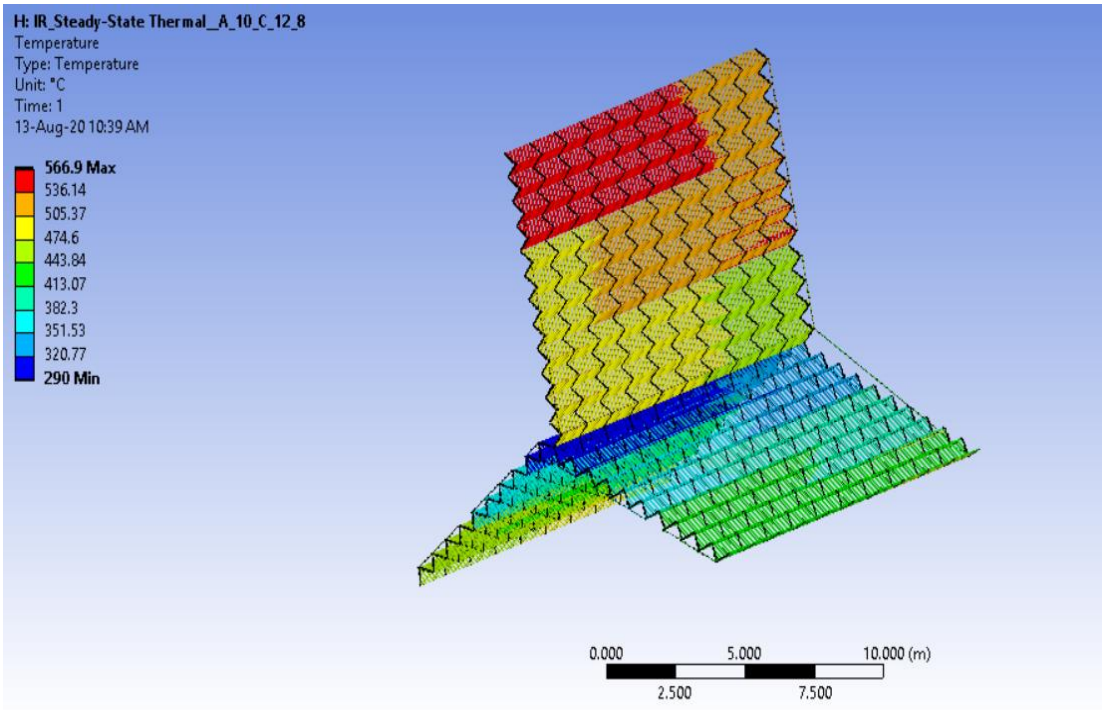

Figure 31: Temperature of flow threads.

6.2.1 The efficiency of the receiver

The thermo-optical efficiency of the receiver is the ratio of power absorbed by the salt to the power incident on the receiver aperture. On the full load condition, thermal analysis is carried out with constant mass flow and the heat flux is scaled in such a way that the outlet temperature of the salt is 565 °C. The thermal losses experienced in the receiver such as radiation and convection losses are also determined, which are further used for the thermo-optical efficiency calculation. α_{abs} is the absorptivity of the solar radiation on the receiver surface, which is used in the calculation to get rid of reflection losses of the absorber tubes.

$$\eta_{thermo-optical} = \frac{P_{abs,\ salt} \times \alpha_{abs}}{P_{abs,\ salt} + L_{IR,\ amb} + L_{Conv,\ amb}} \quad (21)$$

Where
$P_{abs,\ salt}$ = Power absorbed by salt (W)
α_{abs} = Absolute absorptivity (-)
$L_{IR,\ amb}$ = Radiation losses to ambient (W)
$L_{Conv,\ amb}$ = Convection losses to ambient (W)

The analysis of both with and without the radiation enclosures of the receiver is carried out. With the radiation enclosures, some part of the emitted infrared radiation will be absorbed between the neighboring surfaces, but without the enclosures all the emitted radiation will be lost to the atmosphere. The thermo-optical efficiency of the Star receiver is 92 % and 89 % with and without the radiation enclosures respectively. There is around three percent increase in the thermo-optical efficiency of the receiver with enclosures compared to without enclosures. The peak flux is increased from 1.46 MW/m^2 to 1.49 MW/m^2 to reach the required outlet temperature when the radiation emission between surface to surface is not considered.

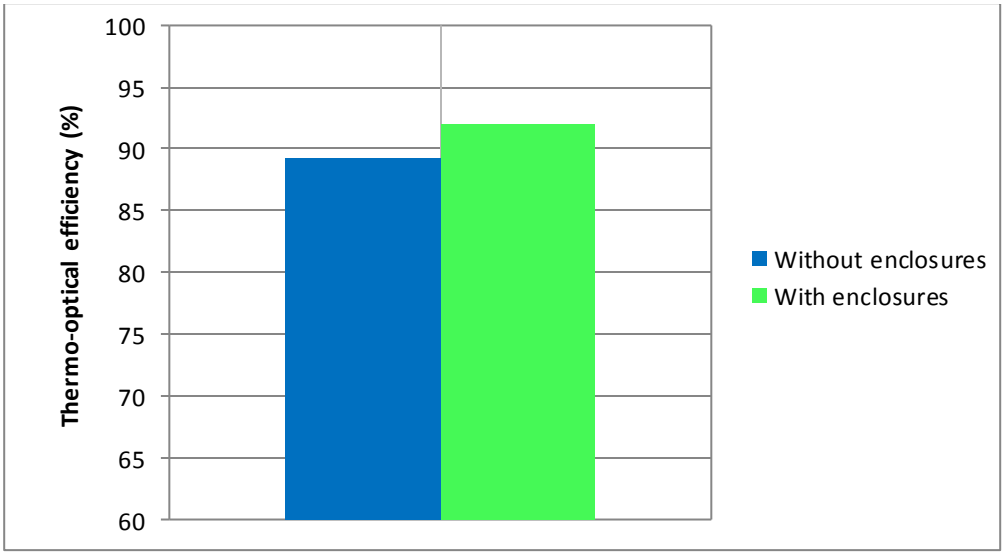

Figure 32: Efficiency with and without enclosures.

6.2.2 Heat losses

After scaling the heat flux densities on the receiver surface to reach the desired outlet temperature (565 °C), the convection and radiation losses from the receiver surface to the atmosphere are determined in ANSYS and the amount of solar radiation reflected by the receiver is obtained from SPRAY results. The thermal analysis in ANSYS is carried out for both with and without the radiation enclosures. As the radiation losses are high without the enclosures, so peak flux should be increased to get the required output power and the temperature of salt. The convective, reflection losses are 7.6 MW and 24 MW respectively, and radiative losses with and without the enclosures are 17.5 MW and 34.8 MW respectively. The radiative losses with the enclosures are less compared to without enclosures because with the enclosures, the heat radiation will not be emitted directly to the atmosphere from the absorber tubes rather some part of the emitted radiation will be incident or reflected between the neighboring tubes and gets absorbed. The radiative losses are reduced by around 50 % with the addition of radiation enclosures in ANSYS. The convection losses account for 1.25 % of the incident power and the solar reflection losses are about 4 % because the absolute absorptivity of the Star receiver is 96 %. There are no conduction losses in the Star receiver because there is no insulation layer compared to the External receiver. From the total incident power on the receiver aperture, around 8 % losses accounts for reflection, convection and radiation with the radiation enclosures and the remaining 92 % of power, absorbed by the salt.

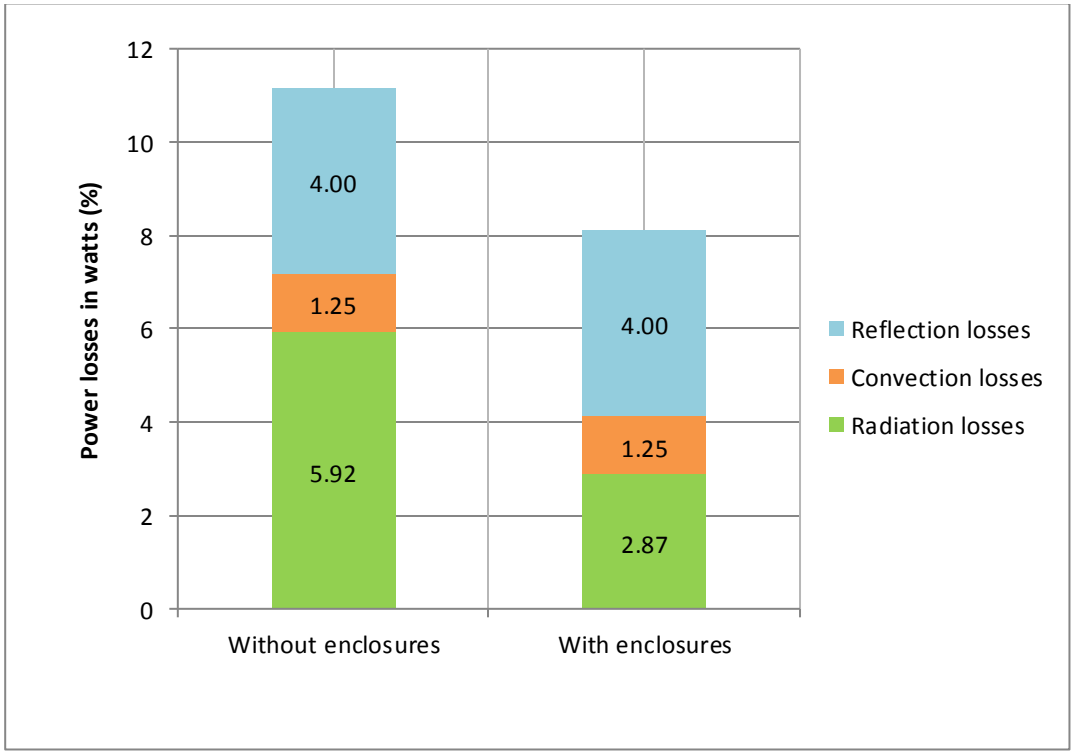

Figure 33 : Heat losses in the receiver.

6.2.3 Receiver efficiency as a function of solar load

The present simulations yielded a thermo-optical efficiency of the Star receiver of 92 % under full load condition. Under weather conditions such as sunrise, sunset and during cloudy condition, the solar radiation reflected by the heliostats on to the receiver is decreased. So, the flux densities on the receiver will be reduced and the power absorbed by the salt also decreases. To execute this condition during the analysis in ANSYS, the heat flux on the receiver surface is kept constant based on the interested load condition. Based on the load condition, the outlet temperature of the heat transfer medium is maintained at 565 °C by scaling the mass flow input in the receiver and then the thermal losses of the receiver are determined. The thermo-optical efficiency of the receiver keeps reducing as the solar load is decreased as shown in Figure 34, but the efficiency is maintained above 80 % even with a minimum load of 20 %. The Star receiver efficiency is over 90 % in between 60 to 100 % load condition. At 40 % solar load, the efficiency is 88 % which is the efficiency of the External receiver at full load condition.

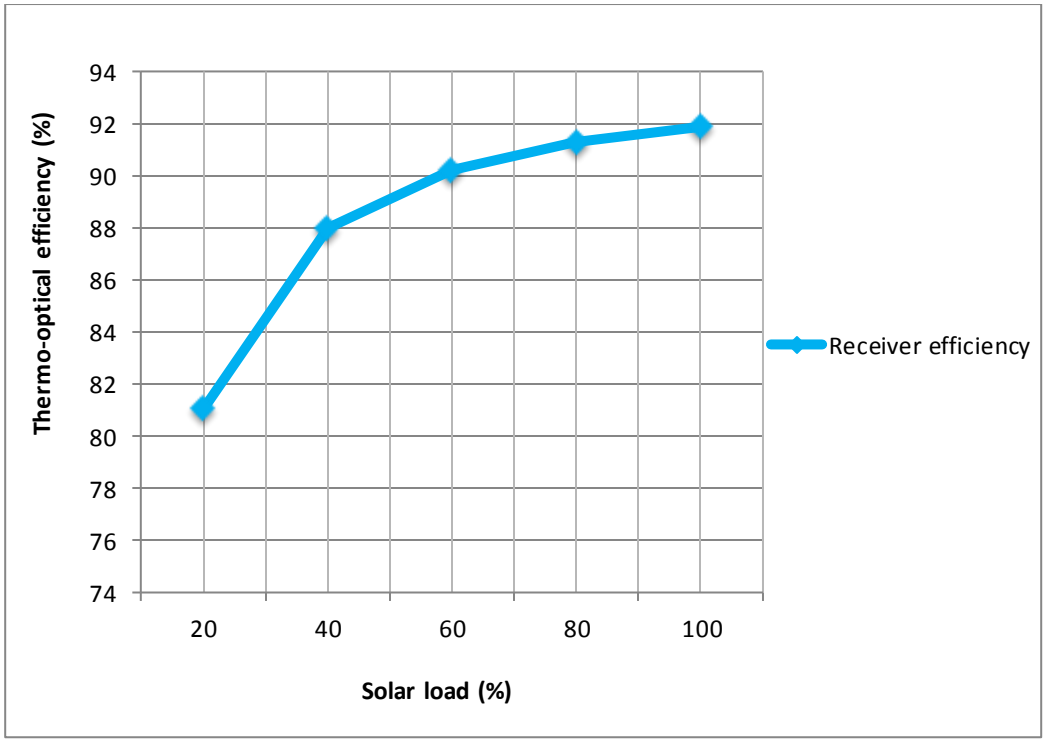

Figure 34: Receiver efficiency as a function of solar load.

The radiation and convection losses to the atmosphere are slightly decreased in magnitude as the load is decreased, due to the reduction in surface temperature of the receiver. But the percentage of thermal losses in Figure 35 drastically increased because of decrease in the incident power on the receiver during part loads. And also, the power absorbed by the salt is decreased. The reflection losses are independent of the incident power because the reflection losses are dependent on the geometry of the receiver and the material absorptance, so the reflection losses are constant in all loads.

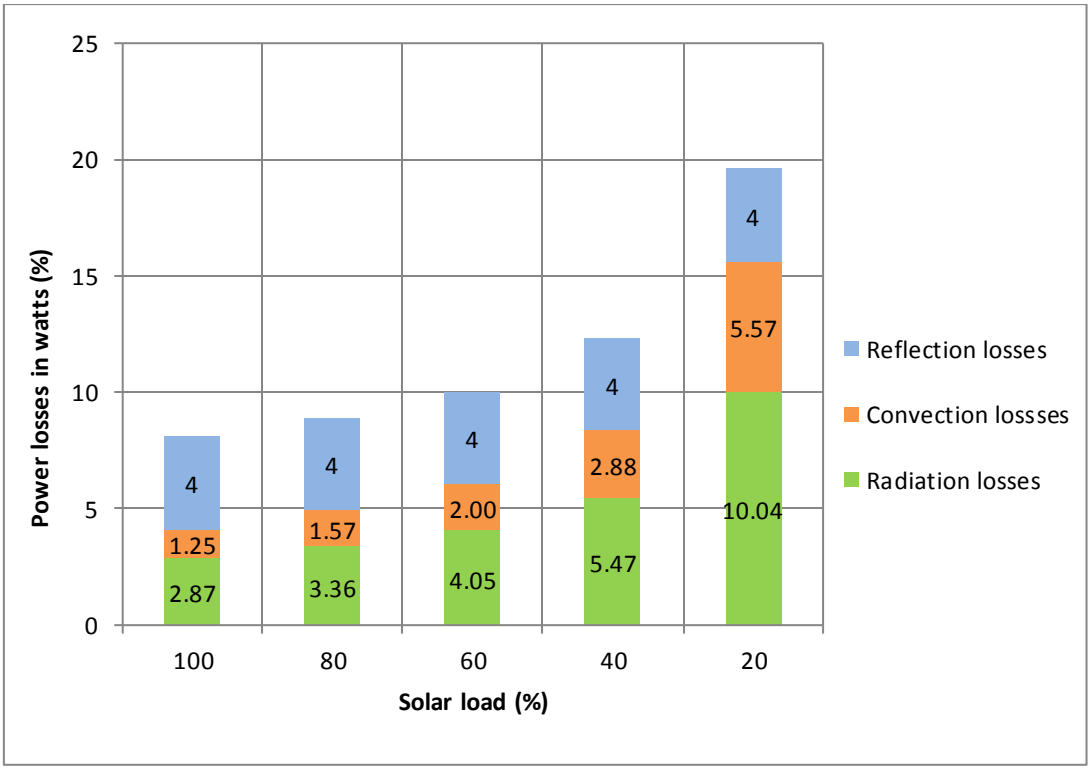

Figure 35: Losses during part load.

6.2.4 Receiver efficiency as a function of wind velocities

Receivers are operated under 20 m/s wind velocities as described in chapter 4.3.2. The heat transfer coefficients are obtained as a function of wind velocities around the receiver. Uhlig et al. [19] deduced the convective heat transfer coefficients of Star receiver with respect to wind velocities through CFD analysis, so the heat transfer coefficients corresponding to these wind velocities are obtained from this study. The solar load study is carried out for 0 and 20 m/s wind velocities around the absorber tubes of the receiver and for 20 m/s without the fins in between the absorber tubes by varying convection coefficient to ambient as shown in Figure 36. At design point up to 20 m/s wind velocity with the fins in between the absorber tubes, the receiver efficiency is above 90 % achievable. With a minimum load of 20 %, the thermo-optical efficiencies are above 80 % and 74 % at 0 m/s and 20 m/s respectively. The receiver efficiency is maintained above 90 % in between 60-100 % solar load under zero wind loads. In both cases, a minimum receiver efficiency of 85 % is achievable when the solar load is more than 40 %.

In case of 20 m/s wind velocity without the fins, the thermo-optical efficiency of the receiver is 86 % and convection losses are increased by 7 % compared to the losses with the fins at full load condition. Mainly convection losses to the ambient are increased drastically because wind can be passed in between the absorber tubes. At 20 % load, the receiver efficiency is 55 %, which is 20 % less than the efficiency of the receiver operating 20 m/s with the fins.

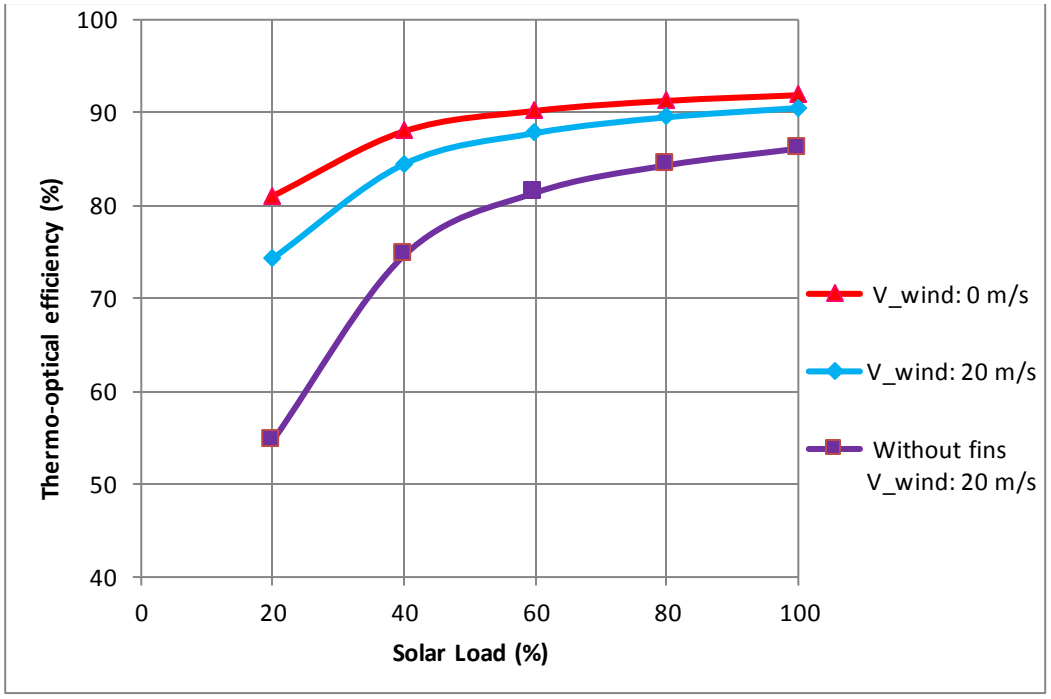

Figure 36: Receiver efficiency as a function of solar load and wind velocity.

In Figure 37, the power losses under the wind loads around the receiver are plotted at full load condition. At higher wind velocities, the convection losses to the ambient are increased significantly, and the radiation and reflection losses are independent of wind velocities. Especially without the fins, the convection losses are relatively high. In the current design of the Star receiver, the fins are included to have a better structural integrity, which also reduce convection losses to the atmosphere.

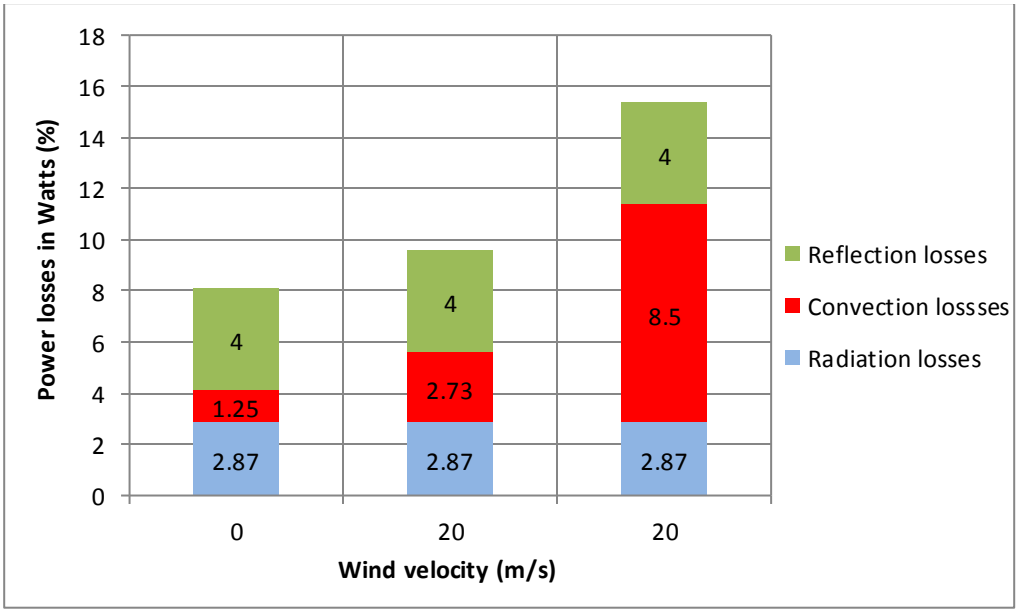

Figure 37: Losses based on wind velocities.

6.3 Overall thermo-optical efficiency

The overall thermo-optical efficiency is the ratio of power absorbed by the salt to the power entering the receiver region. The thermo-optical efficiency of the Star receiver is 79 % on full load condition. The efficiency is quite low mainly due to higher spillage losses. Overall thermo-optical efficiency of the receiver can be improved by reducing the spillage losses which can be achievable with the optimized heliostats aiming on the receiver surface.

$$\eta_{\text{thermo}-\text{optical}} = \frac{P_{\text{abs, salt}}}{P_{\text{RecReg}}} \tag{22}$$

Power reaching the receiver region	712	MW
Power absorbed by the salt	560	MW
Overall thermo-optical efficiency	79	%

Table 13: Efficiency of the Star receiver.

7 Comparison and discussion

Here the thermo-optical efficiencies of the Star receiver (560 MW) are compared with the External receiver (700 MW) operating at 0 m/s and 20 m/s wind loads. On full load condition, the thermo-optical efficiencies of the Star receiver are over 90% in both the cases. There is almost 5 % increase in efficiency of the Star receiver compared to the External receiver operating at 0 m/s at all load points. The efficiencies of the Star receiver operating under both the velocities are comparatively more than the External receiver operating under zero wind loads in between 40 – 100 % solar load. At 20 – 40 % load condition, the efficiency of Star receiver operating 20 m/s is equal to the External receiver operating at 0 m/s. When both the receivers are operating 20 m/s,

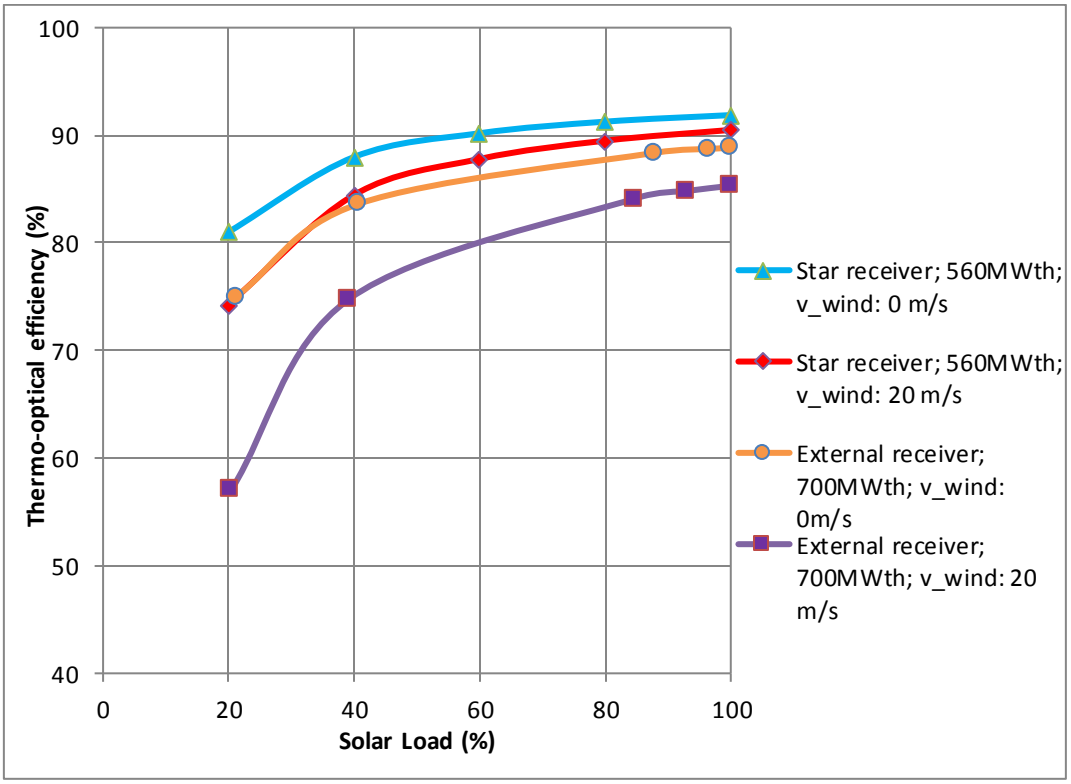

Figure 38: Thermo-optical efficiencies of Star and External receiver [16].

At full load condition, the power losses in Star and External receiver is shown in Figure 39. The infrared radiation losses to ambient in Star receiver are 1.6 % less than External receiver because the local radiation view factor of Star receiver (0.766) is less than the External receiver (1). The view factor of the External receiver is 1 to ambient because the surface is flat to ambient, so all emitted radiation from the absorber surface will be lost to the atmosphere, whereas in the Star receiver only 76 % radiation will be reflected to the atmosphere remaining 24 % of radiation will be reflected between the neighboring tubes and gets absorbed. Convective losses to ambient are 1.25 % and 1.30 % in Star and External receivers

respectively, the losses are less in Star receiver due to lower convective heat transfer coefficients. The reflective losses in Star receiver are reduced by 43 % in comparison to External receiver due to higher solar absorptivity. There are no conduction losses in the Star receiver because there is no insulation on the backside of the tubes as in the External receiver, which accounts around 0.02 %.

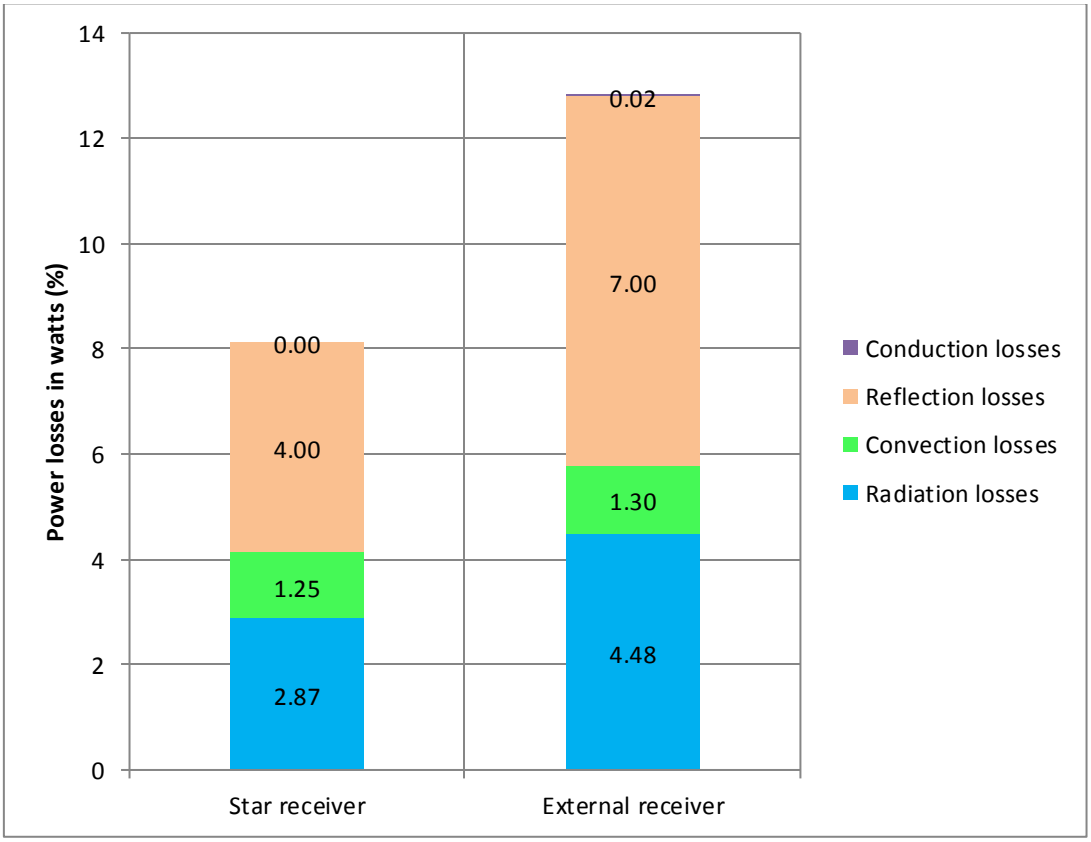

Figure 39: Losses in Star and External receiver.

8 Conclusion

The thermo-optical performance of a new receiver design known as Star receiver is analyzed in this work. A steady state thermal FEM model of the receiver coupled to a raytracing model has been developed. The raytracing is carried out in SPRAY software to determine the heat flux densities distribution on the receiver model and the optical losses such as reflection and spillage losses. Thermal analysis of the Star receiver is carried out in ANSYS Software to determine the temperature distribution and the heat losses such as convection and radiation losses to the ambient. Then the thermo-optical efficiency of the Star receiver is evaluated.

Based on the solar radiation reflected by the heliostats, the heat flux densities on the receiver surface are obtained through optical simulation. The power incident on the receiver aperture to the power reaching the receiver region is known as intercept efficiency which is 85.4 % in the Star receiver and the remaining 14.6 % power losses are due to spillage. The solar absorptance of the Star receiver is 96 % and the remaining losses are due to the reflection of absorber tubes in the receiver. The spillage losses are high in Star receiver compared to 3-5 % spillage in External receiver and these losses can reduced by optimizing the heliostats aiming on the receiver. The reflection losses are reduced by 3 % in Star receiver in contrast to External receiver.

The heat flux on the receiver surface is scaled in such a way that the outlet temperature of the nitrate salts is 565 °C, a peak heat flux of 1.46 MW/m^2 is required which is higher than the External receiver (1.12 MW/m^2) and must be further optimized in order to adhere to structural limits of the absorber tubes. The radiation and convection losses to ambient are 2.87 % and 1.25 % respectively. The thermo-optical efficiency of the Star receiver is 92 % which is better than External receiver (88 %) because the losses such as reflection, radiation and convection losses to the atmosphere are reduced by 3 %, 1.6 % and 0.05 % respectively, compared to the External receiver. Even during part load conditions and under different wind velocities, higher efficiencies are achieved in case of the Star receiver. However, the overall thermo-optical efficiency of the Star receiver is 79 % is less than the External receiver (86 %), which can be enhanced by reducing the spillage losses.

The future aspects of the Star receiver design are to further optimize heliostats aiming on the receiver surface, so that the peak flux densities and spillage losses of the receiver can be reduced. Therefore, the overall thermo-optical efficiency of the receiver would be improved. The structural stability of the geometry configuration of the receiver and thermal stresses developed on the absorber tubes due to either side solar irradiation need to be validated.

9 Bibliography

[1] D. Barley, R. Vidu and P. Stroeve, "Innovation in concentrated solar power," *Solar Energy Material ans Solar Cells,* vol. 95, pp. 2703-2725, 2011.

[2] J. I. Ortega, J. I. Burgaleta and F. M. Téllez, "Central Receiver System Solar Power," *Journal of Solar Energy Engineering,* vol. 130, 2008.

[3] C. Frantz, A. Fritsch and R. Uhlig, "Advanced Solar Tubular Receiver Design (ASTRID): A powerful tool for receiver design and optimization," 2016.

[4] J. I. Burgaleta, S. Arias and a. D. Ramirez, "Gemasolar, The First Tower Thermosolar Commercial Plant with Molten Salt Storage".

[5] C. K.Ho, "Advances in central receivers for concentrating solar applications".

[6] C. Frantz, "HPMS – AP3: Receiverbewertung".

[7] "SolarPACES," [Online]. Available: https://www.solarpaces.org/how-csp-works/. [Accessed 27 08 2020].

[8] H. Zhang, J. Baeyens, J. Degreve and G. Caceres, "Concentrated solar power plants: Review and design methodology," *Renewable and Sustainable Energy Reviews,* pp. 466-481, 2013.

[9] "The National Renewable Energy Laboratory," [Online]. Available: https://solarpaces.nrel.gov/by-technology/power-tower. [Accessed september 2020].

[10] B. E. a. D. Gillb, "Evaluation of annual efficiencies of high temperature central," SolarPACES , 2013.

[11] M. J. Emes, M. Arjomandi and G. J. Nathan, "Effect of heliostat design wind speed on the levelised cost of electricity from concentrating solar thermal power tower plants," Adelaide, Australia, 2015.

[12] S. M. Besarati, D. Y. Goswami and E. K. Stefanakos, "Optimal heliostat aiming strategy for uniform distribution of heat flux on the receiver of a solar power tower plant," *Energy Conversion and Management,* vol. 84, pp. 234-243, 2014.

[13] J. M. Lata, M. Rodríguez and M. Á. d. Lara, "High Flux Central Receivers of Molten Salts for the New Generation of Commercial Stand-Alone Solar Power Plants," *Journal of Solar Energy Engineering,* vol. 130, 2008.

[14] L. L. Vant-Hull, "The Role of ‘‘Allowable Flux Density’’ in the Design and Operation of Molten-Salt Solar Central Receivers," *Journal of Solar Energy Engineering,* vol. 124, pp. 165-169, May 2002.

[15] H. benoit, L. Spreafico, D. Gauthier and G. Flamant, "Review of heat transfer fluids in tube-receivers used in concentrating solar thermal systems".

[16] M. Puppe, S. Giuliano, C. Frantz, R. Uhlig and R. Flesch, "Techno-Economic Optimization of Molten Salt Solar Tower," in *SolarPACES*, 2017.

[17] C. Frantz, C. Schwager and M. Aust, "Stand der Technik - Salzschmelze-Receiver".

[18] M. Rodríguez-Sánchez, A. Sánchez-González, C. Marugán-Cruz and D. Santana, "New designs of molten-salt tubular-receiver for solar power tower," *Energy Procedia,* vol. 49, pp. 504 - 513, 2014.

[19] C. F. Ralf Uhlig, "Evaluation of Convective Losses of a Novel External".

[20] K. Cliffhord, J. M. Christian, J. Yellowhair, J. Ortega and C. Anderka, "Fractal-Like Receiver Geometries and Features for Increased Light Trapping and Thermal Efficiency," American Institute of Physics, Albuquerque, 2016.

[21] J. E. Pachaeo., "Final test and evaluation results from the Solar two project," in *Sandia National Laboratories*, Albuquerque, New Mexico, 2002.

[22] M. J. Niemeier, "Potenzialbewertung eines neuartigen Rohr-Receiver-Designs für Solarturmkraftwerke mit Flüssigsalzen," 2018.

[23] J. M. Christian, J. D. Ortega, C. K. Ho and J. Yellowhair, "Design and Modeling of Light-Trapping Tubular Receiver Panels," in *ASME*, 2016.

[24] R. I. Olivares, W. Stein and P. Marvig, "Thermogravimetric Study of Oxidation-Resistant Alloys," *JOM,* vol. 65, pp. 1660-1668, 2013.

[25] H. Benoit, L. Spreafico, D. Gauthier and G. Flamant, "Review of heat transfer fluids in tube-receivers used in concentrating solar thermal systems: Properties and heat transfer coefficients," *Renewable and Sustainable Energy Reviews,* pp. 298-315, 2016.

[26] W. R. Delameter and N. E. Bergan, "Review of the Molten Salt Electic Experiment: A Solar Central Receiver Project," Sandia National Laboratories, Albuquerque, 1986.

[27] P. K. Falcone, "A Handbook for Solar Central Receiver Design," Sandia National Laboratories Livermore, Livermore, 1986.

[28] T. L. Bergman, A. S. Lavine and F. P. Incropera, in *Fundamentals of Heat and Mass Transfer*, 2011.

[29] O. Zienkiewicz, R. Taylor and J. Zhu, The Finite Element Method: its Basis and Fundamentals, Butterworth-Heinemann, 2013.

[30] N. Hanrieder, S. Wilbert, M. Schroedter-Homscheidt, F. Schnell, D. M. Guevara, R. Buck and S. G. a. R. Pitz-Paal, "Atmospheric Extinction in Simulation Tools for Solar Tower," 2017.

[31] "Special metals - High Performance Alloys Literature," [Online]. Available: https://www.specialmetals.com/tech-center/alloys.html. [Accessed 23 08 2020].

[32] VDI Heat Atlas, Springer, 2010.

[33] R. J. Holl, D. R. Barron and S. Saloff, "Molten Salt Solar-Electric Experiment - Volume 1: Testing, Operation and Evaluation," Electric Power Research Institute, EPRI Project Manager, Solar Power Program, California, 1989.

[34] A. B. Zavoico, "Solar Power Tower Design Basis Document," Sandia National Laboratories, Albuquerque, New Mexico, 2001.

[35] A. Amri, I. Izygon and B. Tedjiza, "Central Receiver Plant Evaluation: III) Themis Receiver subsystem evaluation," Sandia National Laboratories, Livermore, California, 1987.

[36] R. Flesch, H. Stadler, R. Uhlig and B. Hoffschmidt, "On the influence of wind on cavity receivers for solar power towers: An experimental analysis," *Applied Thermal Engineering 87,* pp. 724 - 735, 2015.

10 Appendix

10.1 Mesh

The mesh is carried out by increasing number of elements along the axial and circumferential direction of the tube. The element types in the model are prism elements and hexahedral elements also known as a brick element.

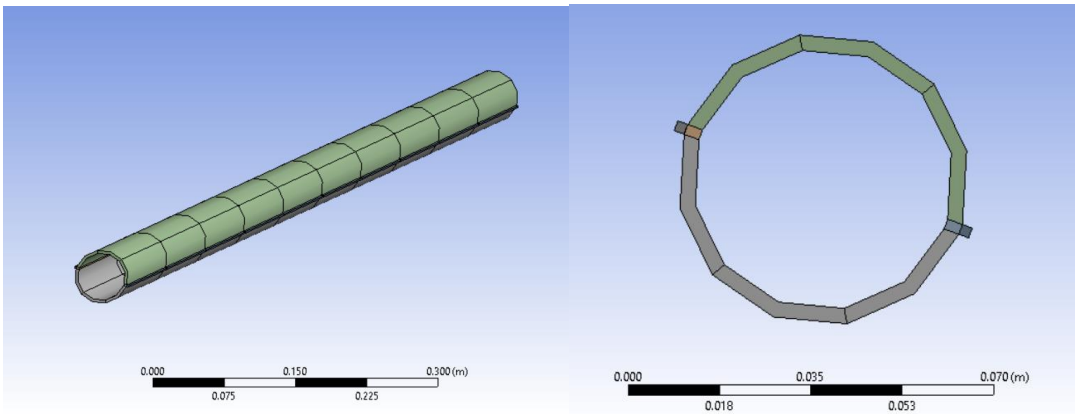

Figure 40: Mesh along axial and circumferential direction.

10.2 Heat transfer coefficients

The heat transfer coefficients which are imported in each absorber panel of the receiver are as shown below.

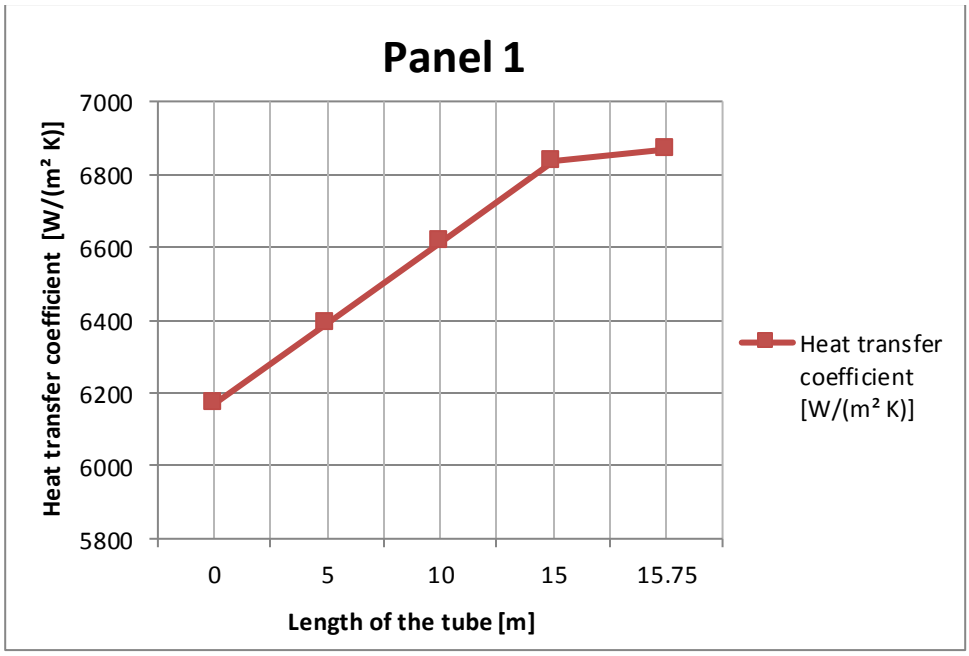

Figure 41: Heat transfer coefficients of panel 1.

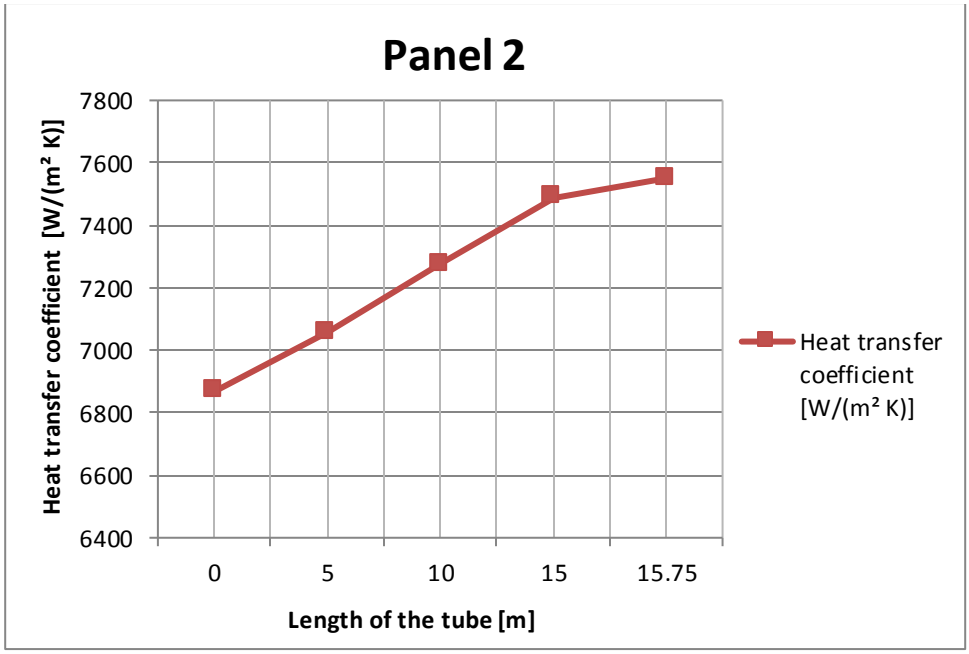

Figure 42: Heat transfer coefficients of panel 2.

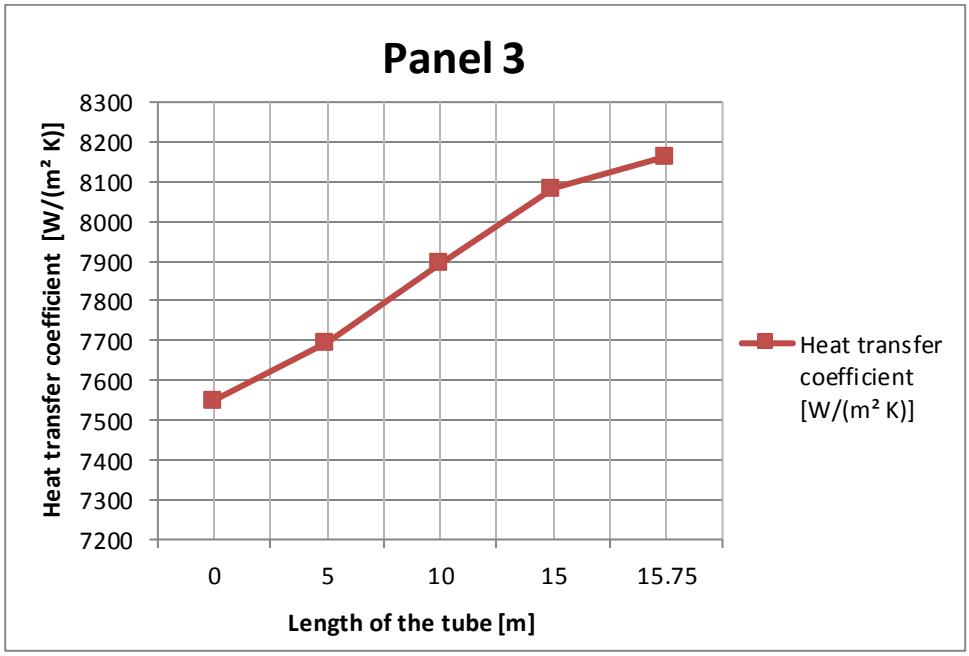

Figure 43: Heat transfer coefficients of panel 3.

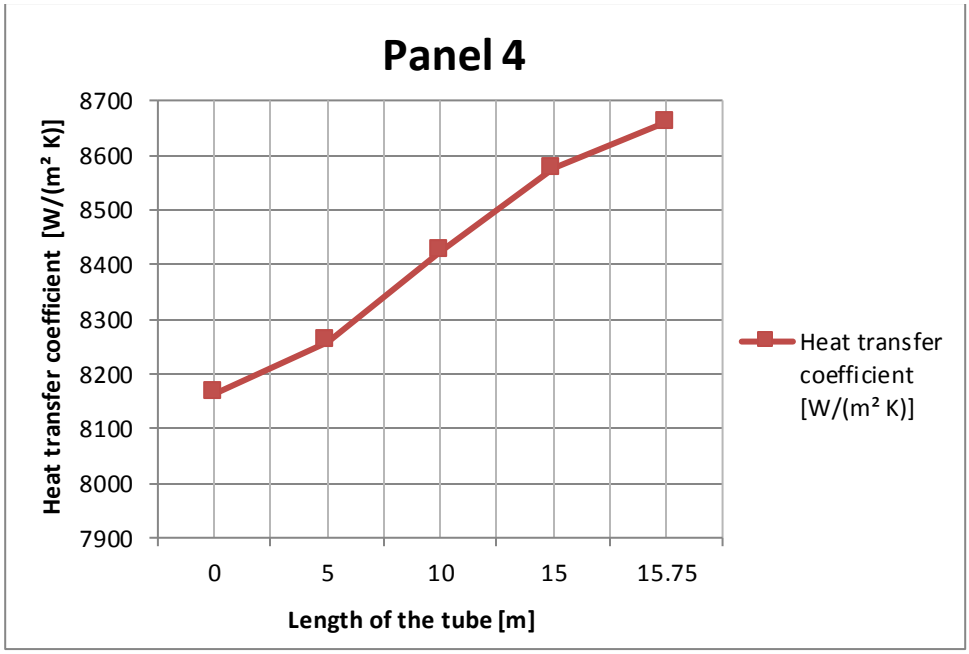

Figure 44: Heat transfer coefficients of panel 4.

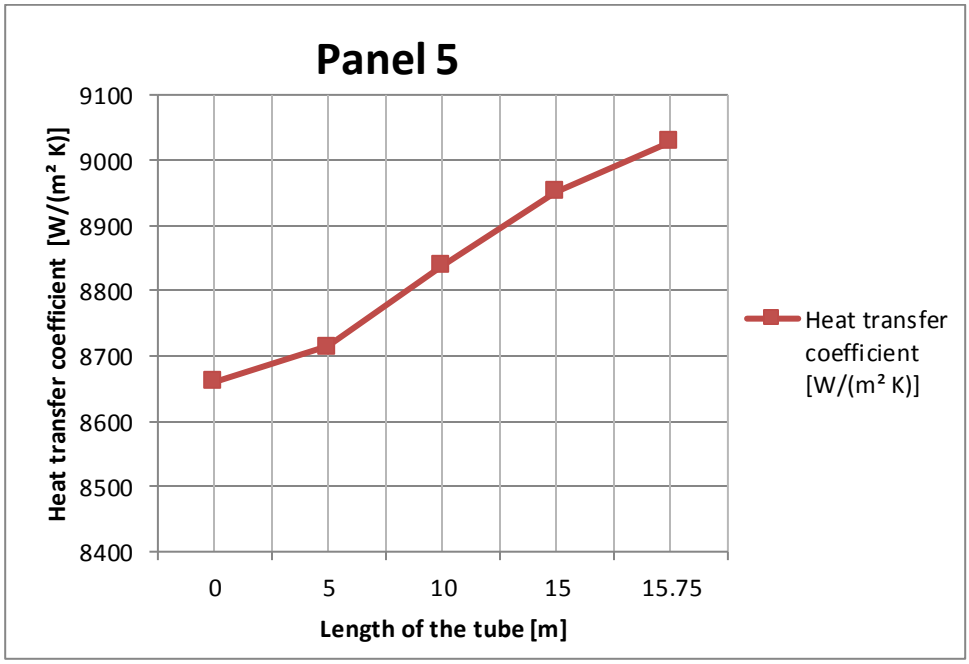

Figure 45: Heat transfer coefficients of panel 5.

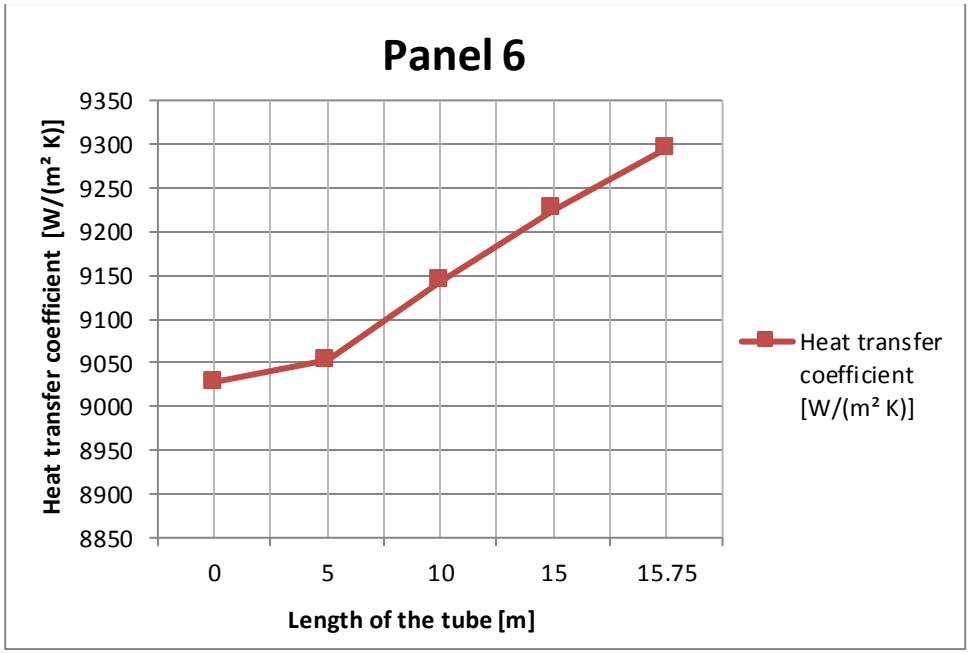

Figure 46: Heat transfer coefficients of panel 6.

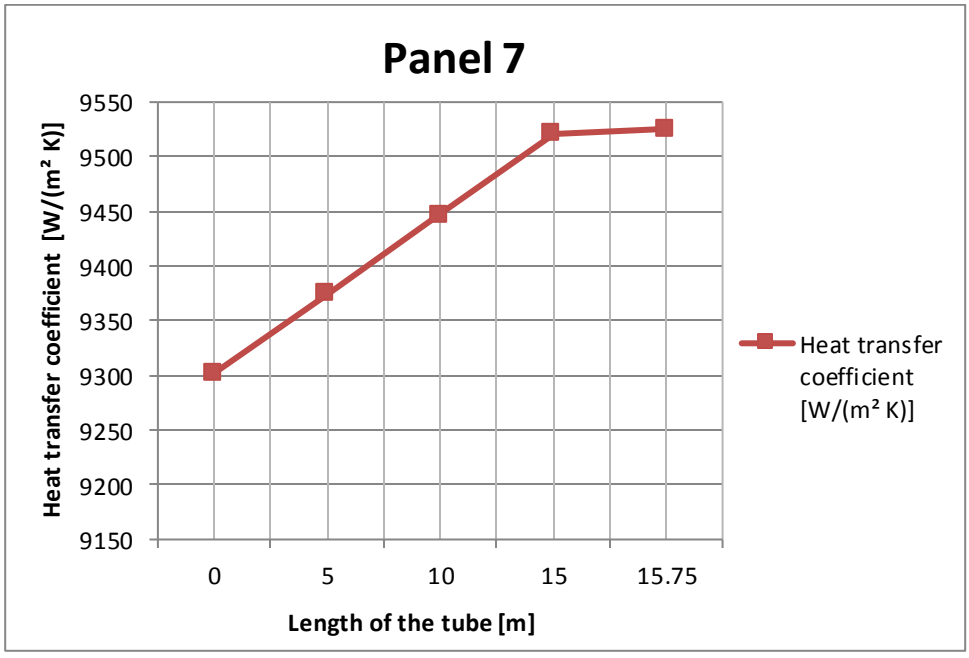

Figure 47: Heat transfer coefficients of panel 7.

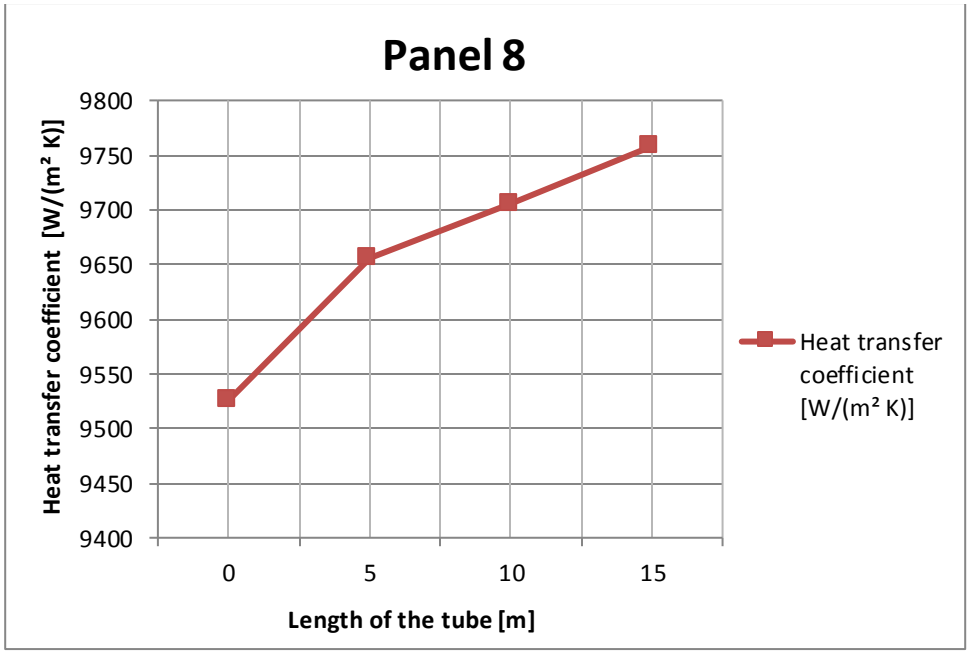

Figure 48: Heat transfer coefficients of panel 8.